Title: Monosomes actively translate synaptic mRNAs in neuronal processes

Authors: Anne Biever[1][†], Caspar Glock[1][†], Georgi Tushev[1], Elena Ciirdaeva[1], Tamas Dalmay[1], Julian D. Langer[1,2], Erin M. Schuman[1*]

Affiliations:
[1]Max Planck Institute for Brain Research, Frankfurt, Germany
[2]Max Planck Institute of Biophysics, Frankfurt, Germany

[†] contributed equally
* to whom correspondence should be addressed:
erin.schuman@brain.mpg.de

Abstract:

In order to deal with their huge volume and complex morphology, neurons localize mRNAs and ribosomes near synapses to produce proteins locally. A relative paucity of polyribosomes (considered the active sites of translation) detected in electron micrographs of neuronal processes (axons and dendrites), however, has suggested a rather limited capacity for local protein synthesis. Polysome profiling together with ribosome footprinting of microdissected synaptic regions revealed that a surprisingly high number of dendritic and/or axonal transcripts were predominantly associated with monosomes (single ribosomes). Contrary to prevailing views, the neuronal monosomes were in the process of active protein synthesis (e.g. they exhibited elongation). Most mRNAs showed a similar translational status in the somata and neuropil, but some transcripts exhibited differential ribosome occupancy in the compartments. Strikingly, monosome-preferring transcripts often encoded high-abundance synaptic proteins. These data suggest a significant contribution of monosome translation to the maintenance of the local neuronal proteome. This mode of translation can presumably solve some of restricted space issues (given the large size of polysomes) and also increase the diversity of proteins made from a limited number of ribosomes available in dendrites and axons.

Main text:

RNA sequencing and *in situ* hybridization have revealed the presence of an unexpectedly high number of RNA species in dendrites and/or axons of the CA1 neuropil (*1, 2*) and many studies have documented the local translation of proteins in dendrites and/or axons (*3-5*). During mRNA translation multiple ribosomes can occupy an individual mRNA (called a "polysome") resulting in the generation of multiple copies of the encoded protein. Polysomes, usually recognized in electron micrographs as a cluster comprising 3 or more ribosomes, have been detected in neuronal dendrites (*6, 7*) but are surprisingly infrequent (e.g. < 0.5 polysomes per μm, see (*7*)) given the diversity of mRNAs present in dendrites and axons (*8*). In neuronal processes, the features and mechanisms of translation have not been explored in detail, in part because of the relative inaccessibility of the dendrites and axons in the neuropil. In particular, how diverse proteins might be synthesized from a limited population of polysomes present in small synaptic volumes is an open question.

Monosomes are the predominant ribosome population in neuronal processes

To visualize the capacity for protein synthesis in the neuropil *in vivo*, we labeled the *de novo* proteome using puromycylation (*9, 10*). We infused puromycin directly into the lateral ventricle of mice, waited 10 min, and then visualized newly synthesized proteins in hippocampal pyramidal neurons by co-immunofluorescence labeling of nascent protein (anti-puromycin antibody) and CA1 pyramidal neurons (anti-wolframin antibody; Wfs1). As expected, we detected an intense nascent protein signal in the somata layer (*stratum pyramidale*), comprising the cell bodies of pyramidal neurons (Fig. 1A, fig. S1A). There was also strong nascent protein evident throughout the dendrites of pyramidal neurons in the neuropil (*stratum radiatum*) (Fig. 1A, fig. S1A). Co-injection of a protein synthesis inhibitor (anisomycin) abolished the nascent protein signal. Because of the very short window of metabolic labeling, these data indicate that protein synthesis also occurs in dendrites *in vivo*.

Polysome profiling is a biochemical fractionation method that allows one to examine the degree of ribosome association of a transcript, i.e. associated with a monosome (single ribosome) or a polysome (multiple ribosomes loaded on an mRNA) (*11*). Using polysome profiling, we examined the ribosome occupancy of transcripts in the hippocampus comparing somata and neuropil that were microdissected from *ex vivo* adult rat hippocampal slices (area CA1; Fig. 1B). Western blot analysis confirmed that the microdissected neuropil was strongly de-enriched for neuronal cell bodies (fig. S1B and C). We obtained a typical polysome profile with two ribosomal subunit peaks (40S and 60S), one monosome (single ribosome, 80S) peak and multiple polysome peaks. No signs of altered polysome integrity (such as a shift towards lower ribosome occupancy) were observed. We assessed the relative association of transcripts with monosomes or polysomes (M/P ratio) in the somata and neuropil by measuring the area under the curve (AUC) of the corresponding absorbance peaks. While a large proportion of mRNAs were associated with polysomes in the somata (Fig. 1C), the M/P ratio was greater than two-fold higher in the neuropil (Fig. 1D and E). The increased M/P ratio observed in the neuropil

resulted from a decrease in polysome abundance when compared to the somata (fig. S1D). As expected, the M/P ratios in whole (non-microdissected) hippocampi (0.56±0.04), comprising cell bodies and neuronal processes, occupied a position between the values obtained for the somata (0.30±0.03) and neuropil (0.76±0.19) (fig. S1E, Fig. 1C and D), further demonstrating that the microdissection procedure does not disrupt polysome stability.

To confirm the difference in the M/P ratios between somata and neuronal projections, we used a well-established *in vitro* system to enrich for cell bodies and neuronal processes (*12*). Rat neurons were cultured on microporous membranes allowing the dendrites and axons (but not cell bodies) to extend to the area beneath the membrane (Fig. 1F, fig. S1F to I). After 21 days *in vitro*, we separately harvested the cell bodies and dendrites/axons and again conducted polysome profiling. Consistent with the microdissected slice data, the M/P ratio was again significantly higher in neurites compared to cell bodies, in part owing to a decreased number of polysomes in the neurite layer (Fig. 1G to I, fig. S1J).

Monosomes actively elongate transcripts in the synaptic neuropil

In mammalian cells, polysomes are thought to represent the translationally active ribosome population (*13-15*). In contrast, monosomes, reflecting single ribosomes detected on transcripts, are presumed to represent the isolation of protein synthesis initiation and termination events, but not active protein synthesis (e.g. the elongation of the polypeptide chain). We compared the translational status of somatic or neuropil-localized monosomes and polysomes by precisely mapping the position of the ribosome(s) along the mRNA using ribosome profiling (*16*) (Fig. 2A). Monosomal or polysomal fractions from the rat neuropil or somata were collected; the purity of fractionation was independently demonstrated by the lack of polysome or monosome peak on sucrose gradient profiles from isolated monosomal and polysomal fractions, respectively (fig. S2). Following polysome profiling, ribosomal fractions were digested and monosome or polysome footprint libraries were prepared. After sequencing three replicates of monosome/polysome footprint libraries and aligning the reads to a reference genome (alignment statistics shown in fig. S3A), the classical ribosome profiling quality metrics were assessed (fig. S3). As expected, the monosome and polysome footprints peaked at a length of around 31 nucleotides (representing the area occupied by the ribosome; fig. S3B and C) and exhibited a depletion of read densities in the untranslated regions (UTRs) and introns (fig. S3D and E). The ribosome profiling libraries were highly reproducible between replicates, as shown by the very small within group variance (fig. S3F) and Pearson correlation coefficients > 0.95 for the majority of the samples (fig. S3G).

We examined the positions of the RNA footprints obtained from neuropil monosomes (Fig. 2B) or polysomes (Fig. 2C) across the open reading frame (ORF) of transcripts. Both the monosome and polysome footprint coverage peaked at the 5' ORF (near/at the translation initiation site); monosome footprints decreased more sharply than polysome footprints over the first 25% of the ORF before reaching a plateau. Only the monosome sample exhibited a pronounced enrichment of footprint reads around the stop codon, presumably

reflecting the position of terminating ribosomes. This pattern is in good agreement with previously published metagene analyses of monosome and polysome footprint densities in yeast (*17*) thus confirming the purity of isolated monosomal and polysomal fractions. Surprisingly, however, a large fraction of monosome footprints occupied the center of the ORF, demonstrating that the localized monosomes are engaged in peptide elongation. A similar pattern was evident for the monosome (and polysome) footprint coverage in the somata (fig. S4A and B) and the whole (non-microdissected) hippocampus (fig. S4C and D; representative polysome profile shown in fig. S1E), indicating that the mid-ORF monosome footprints were not a result of altered polysome integrity during the microdissection procedure.

As the somata and neuropil not only comprise neurons but also glia and interneurons (fig. S5A), we developed a strategy to investigate the translational status of monosomes and polysomes in hippocampal excitatory neurons. In particular, we identified the translatome (ribosome-associated mRNAs) of select hippocampal excitatory neuron populations by combining RiboTag immunoprecipitation (RiboTag-IP) (*18*) with RNA-sequencing (fig. S5B and C). Using differential expression analysis (*19*), we identified transcripts enriched in the RiboTag-IP from hippocampi of Camk2Cre::RiboTag mice (fig. S5D and E) or microdissected somata (fig. S5D and F) and neuropil (fig. S5D and G) of Wfs1Cre::RiboTag mice. Combining the three datasets, we obtained a comprehensive list of 5069 mRNAs ("neuronal" transcripts) selectively translated in cell bodies and processes of excitatory hippocampal neurons (fig. S5H). The relative enrichment and de-enrichment of neuronal and glia/interneuron-related genes, respectively, was validated using a previously published dataset (fig. S5I) (*20*). These data were used to obtain a filtered list of neuronal footprint reads in monosome or polysome libraries from the somata and neuropil (Fig. 2D). As observed above, a significant fraction of neuronal transcripts displayed coverage in the elongating portion of the ORF in the monosome and the polysome samples of both neuropil (fig. S6A and B) and somata (fig. S6C and D). The neuropil-derived monosome (Fig. 2E) and polysome (fig. S6E) footprints exhibited 3-nucleotide phasing throughout the ORF, reflecting the characteristic codon by codon translocation of the ribosome on its mRNA (*16*). These data indicate that both monosomes and polysomes contribute to the active elongation of transcripts localized to neuronal processes.

Neuropil monosomes predominate on synaptic transcripts

To measure the degree to which a neuropil-localized transcript is translated by monosomes or polysomes, we focused on ribosomes that were undergoing elongation but not initiation or termination using footprints aligned to the center of the ORF (see Methods) in the monosome and polysome footprint libraries. Using DESeq2 (*19*), we identified localized neuronal transcripts preferentially translated by either monosomes or polysomes. In the neuropil, we found 463 transcripts significantly enriched in the monosome- versus 372 transcripts enriched in the polysome fraction (Fig. 3A, Table S1) (By contrast, a greater number of transcripts exhibited a significant enrichment on polysomes in the somata, see fig. S7A; Table S1). When we examined the neuropil footprint

pattern across individual transcripts, we identified transcripts that displayed increased monosome (e.g. *Kif1a*; Fig. 3B) or polysome (e.g. *Camk2a;* Fig. 3C) footprint coverage throughout the entire ORF. There was also a large proportion of transcripts (e.g. *Slc17a7*; Fig. 3D) which exhibited equal coverage in monosome and polysome footprint libraries.

Footprints from monosome-enriched mRNAs exhibited strong 3-nucleotide periodicity, reflecting the stepwise movement of active individual ribosomes during the elongation of this transcript subset (Fig. 3E). During translation elongation, however, ribosomes can pause as a result of local RNA structures, the presence of rare codons, interactions between nascent chains or association with trans-regulatory factors (*21-24*). The predominant association of an mRNA with monosomes could thus result from increased pausing at individual codons when compared to the same mRNA's association with polysomes. To test this, for the 463 monosome-enriched transcripts, we computed a pause score by comparing the normalized footprint coverage at individual codons in the monosome and polysome samples (see Methods). We found that most codons did not exhibit significant differences in pausing between the monosome and polysome libraries (Fig. 3F). To further investigate the translational activity status of monosome-preferring transcripts, we used harringtonine (an initiation inhibitor) to analyze a time series of ribosome run-off during elongation (*25*) in hippocampal cultures. Metagene analysis revealed a progressive loss of ribosomes from the 5' end of monosome-preferring transcripts following the harringtonine treatments (fig. S8). Taken together, these findings indicate that monosome-preferring transcripts are actively elongated and do not exhibit differential pausing when associated with single or multiple ribosomes.

What transcript properties influence the neuropil monosome:polysome preference? We detected a positive correlation between the neuropil monosome:polysome preference and ORF length, 3'UTR folding energy and 5'UTR length (fig. S9A, Table S1). On the other hand, a negative correlation was observed between the monosome:polysome ratio and the mean of the typical decoding rate index (MTDR, an estimate of the elongation efficiency (*26*)), GC-content, codon adaption index (CAI) and initiation rate (fig. S9A, Table S1). We also observed an overrepresentation of uORF-containing transcripts (73 mRNAs) among monosome-enriched genes (fig. S9B). Although a previous study in yeast reported that monosomes occupy non-sense mediated decay (NMD) targets (*27*), no relationship was found between the neuropil monosome:polysome preference of transcripts and their likelihood of classification as NMD targets (fig. S9C). An emerging concept is that the fine-tuning of translation rates allows for the optimization of the nascent polypeptide folding during protein synthesis. We thus explored how the monosome:polysome preference related to the structural complexity of the encoded polypeptide. An increased number of secondary structures (α-helix and β-strand) were predicted for monosome-preferring transcripts (fig. S9D). In addition, monosome-preferring transcripts encoded proteins displaying longer structural domains (fig. S9E).

To examine whether particular protein function groups are encoded by monosome- vs. polysome-preferring transcripts in the neuropil, we used gene ontology (GO) (Fig. 3G; see fig. S7B for the somata). Monosome-preferring transcripts exhibited a more significant association with GO terms such as 'synapse', 'vesicle' or 'dendritic tree' than polysome-preferring transcripts in the neuropil. In accordance with this finding, synaptic genes (SynGO annotation (*28*)) displayed higher mean monosome:polysome ratios compared to non-synaptic genes (fig. S10A and B). We found that polysome-preferring transcripts often encode proteins involved in actin cytoskeleton remodeling (Fig. 3G and H). Because functional and morphological changes in synapses rely on the dynamic actin cytoskeleton remodeling (*29*), polysome-translation may be required to supply synapses with high copy numbers of cytoskeletal proteins. Together, these results indicate that, in dendrites and axons, a significant proportion of transcripts important for synaptic function are principally translated by monosomes.

Nature versus nurture of neuronal monosome-translation
To address whether the monosome:polysome preference is intrinsic to the transcript (nature) or influenced by the environment (nurture, i.e. the subcellular compartment), we compared the relative monosome:polysome enrichment of each transcript in the neuropil and somata. We observed a high correlation ($R^2=$ 0.6) between the somata and neuropil monosome:polysome ratios, indicating that a large proportion of transcripts prefer the same type of ribosome occupancy in both compartments (Fig. 4A, monosome-enriched in quadrant 1 or polysome-enriched in quadrant 3). An overlap of the genes classified as monosome- or polysome-preferring in the somata (fig. S7A) and neuropil (Fig. 3A) revealed that many but not all genes exhibited a similar preference between compartments (fig. S11A and B). Using DESeq2 (*19*), we identified transcripts exhibiting significant differences in the monosome:polysome ratio between somata and neuropil (Fig. 4A; Table S1). Only a handful of transcripts (e.g. *Arc* Fig. 4B) exhibited a significantly lower monosome:polysome ratio in the neuropil than somata (Fig. 4A, purple dots, Fig. 4C). The majority of transcripts (e.g. *Serpini1* Fig. 4D) with differential ribosome occupancy between compartments displayed significantly elevated monosome:polysome fold-changes in the neuropil (Fig. 4A, cyan dots, Fig. 4E). Overall we observed a significant shift towards a higher monosome preference in the neuropil (Fig. 4F, fig. S11C). Notably, we also identified some transcripts with opposing monosome:polysome ratios between somata and neuropil (i.e. monosome-preferring in one compartment and polysome-preferring in the other), some of which are key regulators of synaptic plasticity (Fig. 4A quadrants 2 and 4, fig. S12, Table S1). Together, our results demonstrate that neuropil-localized transcripts are, in general, more likely to be translated on monosomes than somatic transcripts.

Monosome translation contributes to the neuropil proteome
Individual synapses are small independent information processing units, each endowed with their own complement of proteins, ranging in copy numbers from 10s to a thousand or so (*48-51*). We observed that previously published protein

261 copy numbers in the rat pre- (Fig. 5A, (*51*)) and post-synapse (Fig. 5B, (*48*))
262 were poorly correlated with the neuropil monosome:polysome preference. To
263 understand the contribution of monosome- and polysome-translation to the
264 overall proteome composition, we conducted mass spectrometry of neuropil
265 proteins (see Methods) and estimated their absolute protein abundances using
266 iBAQ (intensity-based absolute quantification) (*52, 53*) (fig. S13A). As might be
267 expected, we observed higher median iBAQ values for proteins encoded by
268 polysome-preferring transcripts when compared to proteins encoded by
269 monosome-preferring transcripts (Fig. 5C; see fig. S14A for the somata). When
270 we examined the relationship between the abundance of neuropil proteins to
271 their respective monosome:polysome ratios, however, we observed a
272 surprisingly weak correlation ($R^2 = 0.021$; *p*-value = 2.944e-11 Fig. 5D; see fig.
273 S14B for the somata). Around half of the 326 proteins encoded by monosome-
274 preferring transcripts exhibited protein abundances that were greater than the
275 average (Fig. 5D, Table S1), indicating that monosome-preferring transcripts
276 can also encode highly abundant proteins. We next examined the properties of
277 the high abundance proteins encoded by monosome-preferring transcripts
278 ("mono-high"; n=177). To investigate whether the "mono-high" protein
279 abundance is related to mRNA abundance in the neuropil, we estimated local
280 transcript levels using RNA-seq (fig. S13B). Consistent with the correlation
281 between the local transcriptome and proteome ($R^2 = 0.26$; *p*-value < 2.2e-16),
282 the "mono-high" genes had higher mRNA levels (Fig. 5E; see fig. S14C for the
283 somata). We then looked at the relationship between "mono-high" protein
284 abundance and local translation rates, a measurement obtained from neuropil
285 total footprint libraries (without biochemical fractionation) (fig. S13C). Perhaps
286 predictably, we observed that "mono-high" transcripts were amongst the most
287 highly translated mRNAs within the neuropil, which agrees with the overall
288 positive correlation between the neuropil proteome and local translatome ($R^2 =$
289 0.33; *p*-value < 2.2e-16) (Fig. 5F; see fig. S14D for the somata). Taken together,
290 these data show that predominantly monosome-translated transcripts
291 contribute to the neuropil proteome composition by encoding a full range of low
292 and high abundance proteins, depending on their expression level and
293 translation rate.
294
295 **Discussion**
296 In the present study, we investigated the translational landscape in neuronal
297 processes and identified local translation on 80S monosomes as an essential
298 source of synaptic proteins. To date, knowledge about the conformation of the
299 translational machinery near synapses has come mostly from electron
300 micrographs. In these studies ribosomes are unambiguously identified when
301 organized as a polyribosome cluster formed by more than three ribosomes (*54*).
302 The sparse distribution of polysomes in dendrites and spines apparent in
303 electron micrographs has led some to suggest that local protein synthesis
304 represents a minor source of synaptic protein under basal conditions (*55*).
305 Indeed, until the recent detection of mRNAs and the machinery needed for their
306 translation (*5, 56, 57*), the inability to identify polysomes in EM images from
307 mature axons led to assertions that mature axons obtain protein via intracellular
308 transport from the soma. Although a previous EM study suggested the putative

visualization of monosomes in dendritic spines (*54, 58*), monosomes have not been identified with certainty, as their small size (10-25nm) makes it difficult to distinguish them from other dark-staining cytoplasmic particles (*54*). A previous study using a fluorescent reporter suggested monosome translation might be associated with sporadic (isolated) translation events in cultured neuron processes (*59*). Here we detected substantial levels of ongoing protein synthesis in the synaptic neuropil *in vivo* and provide direct evidence for the preferential translation of many pre-and post-synaptic transcripts by monosomes. This finding thus bridges the gap between the relative paucity of visualized translational machinery in neuronal processes and actual measurements of local translation.

Dendritic spines and their associated pre-synaptic boutons that comprise the excitatory synapse are small subcellular compartments, often below 100 nm^3 for spines (*60*). The relatively large dimensions of a polysome (~100-200 nm (*7*)), limits the possibilities for high ribosome occupancy in spines and axon terminals. Indeed, each dendritic spine has been estimated to contain, on average, one polyribosome (*6*). The observed low density of polysomes at synapses could be due to a limited pool of available ribosomes in neuronal processes compared to cell bodies. In agreement with this, we observed a decrease in the percentage of rRNA relative to total RNA (fig. S15A) as well as a de-enrichment of ribosomal proteins (fig. S15B) in the neuropil compared to somata. Translation via smaller machines, i.e. monosomes, allows for more protein synthesis sites within synaptic compartments. While polysomes have been reported to move within cells at an average speed of 2 *µ*m/s (*61*), potentially greater mobility of translating monosomes may allow them to patrol and serve a larger number of synapses. Given that one polysome translates a single mRNA resulting in multiple copies of a single protein, the relative scarcity of ribosomes imposes constraints on both the timing and diversity of locally synthesized proteins. We showed that neuropil-localized transcripts exhibit a greater monosome preference than somatic transcripts, potentially allowing for the production of a more diverse set of proteins from a limited pool of available ribosomes at synapses.

We found that monosome-preferring transcripts encode proteins that span a broad range of abundances in the neuropil. Because many synaptic proteins are present at very low copy numbers within the pre- and post-synaptic compartments (e.g. AMPARs; estimated to ~ 15-20 per PSD) (*50*), their local translation by single ribosomes may suffice to maintain or even alter the synaptic activity. We also uncovered a subset of monosome-preferring transcripts that encode surprisingly high-abundance proteins including the scaffolding proteins Bsn and Dlg3. This subset also exhibited increased RNA levels and translation rates within the neuropil. These features might underlie the ability of these monosome-preferring transcripts to encode abundant proteins. On the other hand, predominant polysome-translation was observed for key signaling, scaffolding or cytoskeletal proteins (e.g. Camk2a, PSD95, actin), which are present at very high copy numbers within synapses (*50*). Many studies investigating translational control in synaptic plasticity or neurological disorders have focused their analysis on transcripts that co-sediment with polysomes (*11, 62-64*). Given that monosomes are key contributors to the

357 neuronal translatome, focusing on polysome-associated transcripts may
358 provide only an incomplete picture of translational regulation.
359 We showed that most transcripts exhibited a similar monosome:polysome
360 preference in both somata and neuropil, suggesting that ribosome occupancy
361 is often an intrinsic feature of the transcript. Consistent with this, we detected a
362 positive correlation between the monosome:polysome ratio and ORF length,
363 which agrees with previous studies reporting decreased ribosome density and
364 protein production for long ORFs (*65-69*). In part, this observation can be
365 explained by reduced initiation rates of longer transcripts (r = -0.29; *p-value* <
366 2.2e-16; see also (*70*)). Contrasting observations, however, have been made
367 in yeast, where monosomes preferentially occupy short ORFs (*27*). This
368 discrepancy might be explained by differences in the translational regulatory
369 mode between organisms such as an expansion in the UTR length/complexity
370 during evolution from lower to higher eukaryotes (*2, 71, 72*).
371 We also observed that monosome-preferring transcripts are often subject to a
372 negative translational regulation, with moderate initiation and elongation
373 kinetics. Interestingly, proteins predominantly encoded by monosome-
374 preferring transcripts were not only longer but also structurally more complex.
375 A "quality mode" slow translation of the monosome-preferring transcripts might
376 allow the fine-tuning of co-translational folding events, ensuring the functionality
377 and preventing the aggregation of the encoded proteins. On the other hand, we
378 found that polysome-preferring transcripts displayed increased initiation and
379 elongation rates allowing a more efficient translation. Polysome-preferring
380 transcripts may thus encode proteins of lower structural complexity, which
381 require less *de novo* protein folding fidelity, potentially allowing their translation
382 in a fast "productivity mode" (*73, 74*).
383 Some transcripts exhibited a differential monosome:polysome preference
384 between the somata and neuropil. Neurons differentially localize 5' and/or 3'
385 UTR isoforms between sub-cellular compartments (*2, 56, 75, 76*). Because
386 these *cis*-regulatory mRNA elements regulate initiation efficiency (*71, 72*),
387 neurons may fine-tune their monosome:polysome preference through selective
388 targeting of competitive UTR isoforms between compartments. Interestingly,
389 we found that *Arc*, a previously reported natural NMD target that contains
390 3'UTR introns (*77*), is monosome-preferring in the somata but polysome-
391 preferring in the neuropil. According to the model proposed by Giorgi et al. (*77*),
392 *Arc* may be silenced by NMD in the somata whereas, in the neuropil, synaptic
393 activity could trigger its release from NMD resulting in a translational
394 upregulation (i.e. polysome-translation).
395 Alternatively, differences in the monosome preference between somata and
396 neuropil could also arise from differential localization/activity of specific
397 translational regulators, including RNA-binding proteins (RBPs) (*78, 79*),
398 microRNAs (*80, 81*), initiation/elongation factors (*64, 82-84*) or the ribosome
399 itself (*85*). For instance, the RBP FMRP is thought to inhibit the translation of
400 selective transcripts in neuronal processes by pausing the translocation of
401 polyribosomes or by directly interacting with the RNA-induced silencing
402 complex (*86-88*). Synaptic activity has also been reported to regulate the local
403 translational machinery through changes in the phosphorylation status of
404 initiation (*84*) and elongation factors (*89*). Thus, local activity-induced signaling

405 events can also likely control the flow of ribosomes on an mRNA and dictate its
406 monosome:polysome preference.
407 A rapid up-regulation in the number of polyribosomes has been observed in
408 electron micrographs of dendritic shafts and spines after synaptic plasticity
409 induction (*7*). Our data show that, for many transcripts, monosome translation
410 is the preferred mode of protein synthesis in neuronal processes and
411 presumably satisfies the local demands under basal conditions. The formation
412 of polysomes, however, could be required to supply synapses with *de novo*
413 plasticity-related proteins in response to stimulation. We identified transcripts
414 that prefer the predominant ribosome population present in either somata
415 (polysomes) or neuropil (monosomes) (Fig. 4A, Table S1) and thus represent
416 candidates that may shift towards higher polysome occupancy in response to
417 synaptic stimulation. Additionally, given the spatial limitations within dendritic
418 spines and axonal boutons, synaptic activity could also regulate monosome
419 translation to diversify the local proteome with spatial and temporal precision.
420

421 **References and Notes:**
422 1.   I. J. Cajigas *et al.*, The local transcriptome in the synaptic neuropil
423   revealed by deep sequencing and high-resolution imaging. *Neuron* **74**,
424   453-466 (2012).
425 2.   G. Tushev *et al.*, Alternative 3' UTRs Modify the Localization,
426   Regulatory Potential, Stability, and Plasticity of mRNAs in Neuronal
427   Compartments. *Neuron* **98**, 495-511 e496 (2018).
428 3.   J. M. Cioni, M. Koppers, C. E. Holt, Molecular control of local
429   translation in axon development and maintenance. *Curr Opin Neurobiol*
430   **51**, 86-94 (2018).
431 4.   C. Glock, M. Heumuller, E. M. Schuman, mRNA transport & local
432   translation in neurons. *Curr Opin Neurobiol* **45**, 169-177 (2017).
433 5.   A. S. Hafner, P. G. Donlin-Asp, B. Leitch, E. Herzog, E. M. Schuman,
434   Local protein synthesis is a ubiquitous feature of neuronal pre- and
435   postsynaptic compartments. *Science* **364**, (2019).
436 6.   L. E. Ostroff, J. C. Fiala, B. Allwardt, K. M. Harris, Polyribosomes
437   redistribute from dendritic shafts into spines with enlarged synapses
438   during LTP in developing rat hippocampal slices. *Neuron* **35**, 535-545
439   (2002).
440 7.   L. E. Ostroff *et al.*, Shifting patterns of polyribosome accumulation at
441   synapses over the course of hippocampal long-term potentiation.
442   *Hippocampus* **28**, 416-430 (2018).
443 8.   A. Biever, P. G. Donlin-Asp, E. M. Schuman, Local translation in
444   neuronal processes. *Curr Opin Neurobiol* **57**, 141-148 (2019).
445 9.   A. David *et al.*, Nuclear translation visualized by ribosome-bound
446   nascent chain puromycylation. *J Cell Biol* **197**, 45-57 (2012).
447 10. E. K. Schmidt, G. Clavarino, M. Ceppi, P. Pierre, SUnSET, a
448   nonradioactive method to monitor protein synthesis. *Nat Methods* **6**,
449   275-277 (2009).
450 11. C. Bagni, L. Mannucci, C. G. Dotti, F. Amaldi, Chemical stimulation of
451   synaptosomes modulates alpha -Ca2+/calmodulin-dependent protein

452   kinase II mRNA association to polysomes. *J Neurosci* **20**, RC76
453   (2000).

454 12.   M. M. Poon, S. H. Choi, C. A. Jamieson, D. H. Geschwind, K. C.
455   Martin, Identification of process-localized mRNAs from cultured rodent
456   hippocampal neurons. *J Neurosci* **26**, 13390-13399 (2006).

457 13.   J. R. Warner, P. M. Knopf, The discovery of polyribosomes. *Trends*
458   *Biochem Sci* **27**, 376-380 (2002).

459 14.   J. R. Warner, P. M. Knopf, A. Rich, A multiple ribosomal structure in
460   protein synthesis. *Proc Natl Acad Sci U S A* **49**, 122-129 (1963).

461 15.   J. R. Warner, A. Rich, The Number of Soluble Rna Molecules on
462   Reticulocyte Polyribosomes. *Proc Natl Acad Sci U S A* **51**, 1134-1141
463   (1964).

464 16.   N. T. Ingolia, S. Ghaemmaghami, J. R. Newman, J. S. Weissman,
465   Genome-wide analysis in vivo of translation with nucleotide resolution
466   using ribosome profiling. *Science* **324**, 218-223 (2009).

467 17.   J. W. Chartron, K. C. Hunt, J. Frydman, Cotranslational signal-
468   independent SRP preloading during membrane targeting. *Nature* **536**,
469   224-228 (2016).

470 18.   E. Sanz *et al.*, Cell-type-specific isolation of ribosome-associated
471   mRNA from complex tissues. *Proc Natl Acad Sci U S A* **106**, 13939-
472   13944 (2009).

473 19.   M. I. Love, W. Huber, S. Anders, Moderated estimation of fold change
474   and dispersion for RNA-seq data with DESeq2. *Genome Biol* **15**, 550
475   (2014).

476 20.   A. Zeisel *et al.*, Brain structure. Cell types in the mouse cortex and
477   hippocampus revealed by single-cell RNA-seq. *Science* **347**, 1138-
478   1142 (2015).

479 21.   G. Kramer, D. Boehringer, N. Ban, B. Bukau, The ribosome as a
480   platform for co-translational processing, folding and targeting of newly
481   synthesized proteins. *Nat Struct Mol Biol* **16**, 589-597 (2009).

482 22.   J. B. Plotkin, G. Kudla, Synonymous but not the same: the causes and
483   consequences of codon bias. *Nat Rev Genet* **12**, 32-42 (2011).

484 23.   K. C. Stein, J. Frydman, The stop-and-go traffic regulating protein
485   biogenesis: How translation kinetics controls proteostasis. *J Biol Chem*
486   **294**, 2076-2084 (2019).

487 24.   T. E. Graber *et al.*, Reactivation of stalled polyribosomes in synaptic
488   plasticity. *Proc Natl Acad Sci U S A* **110**, 16205-16210 (2013).

489 25.   N. T. Ingolia, L. F. Lareau, J. S. Weissman, Ribosome profiling of
490   mouse embryonic stem cells reveals the complexity and dynamics of
491   mammalian proteomes. *Cell* **147**, 789-802 (2011).

492 26.   A. Dana, T. Tuller, The effect of tRNA levels on decoding times of
493   mRNA codons. *Nucleic Acids Res* **42**, 9171-9181 (2014).

494 27.   E. E. Heyer, M. J. Moore, Redefining the Translational Status of 80S
495   Monosomes. *Cell* **164**, 757-769 (2016).

496 28.   F. Koopmans *et al.*, SynGO: An Evidence-Based, Expert-Curated
497   Knowledge Base for the Synapse. *Neuron* **103**, 217-234 e214 (2019).

498 29.   R. P. Tas, L. C. Kapitein, Exploring cytoskeletal diversity in neurons.
499   *Science* **361**, 231-232 (2018).

500   30.   A. J. Silva, C. F. Stevens, S. Tonegawa, Y. Wang, Deficient
501   hippocampal long-term potentiation in alpha-calcium-calmodulin kinase
502   II mutant mice. *Science* **257**, 201-206 (1992).
503   31.   G. L. Lyford *et al.*, Arc, a growth factor and activity-regulated gene,
504   encodes a novel cytoskeleton-associated protein that is enriched in
505   neuronal dendrites. *Neuron* **14**, 433-445 (1995).
506   32.   W. Link *et al.*, Somatodendritic expression of an immediate early gene
507   is regulated by synaptic activity. *Proc Natl Acad Sci U S A* **92**, 5734-
508   5738 (1995).
509   33.   C. S. Wallace, G. L. Lyford, P. F. Worley, O. Steward, Differential
510   intracellular sorting of immediate early gene mRNAs depends on
511   signals in the mRNA sequence. *J Neurosci* **18**, 26-35 (1998).
512   34.   O. Steward, P. F. Worley, Selective targeting of newly synthesized Arc
513   mRNA to active synapses requires NMDA receptor activation. *Neuron*
514   **30**, 227-240 (2001).
515   35.   T. Bacaj, M. Ahmad, S. Jurado, R. C. Malenka, T. C. Sudhof, Synaptic
516   Function of Rab11Fip5: Selective Requirement for Hippocampal Long-
517   Term Depression. *J Neurosci* **35**, 7460-7474 (2015).
518   36.   P. B. Allen, A. T. Greenfield, P. Svenningsson, D. C. Haspeslagh, P.
519   Greengard, Phactrs 1-4: A family of protein phosphatase 1 and actin
520   regulatory proteins. *Proc Natl Acad Sci U S A* **101**, 7187-7192 (2004).
521   37.   J. Y. Kim *et al.*, Different expression patterns of Phactr family members
522   in normal and injured mouse brain. *Neuroscience* **221**, 37-46 (2012).
523   38.   H. Wang *et al.*, Norbin is an endogenous regulator of metabotropic
524   glutamate receptor 5 signaling. *Science* **326**, 1554-1557 (2009).
525   39.   B. Tews *et al.*, Synthetic microRNA-mediated downregulation of Nogo-
526   A in transgenic rats reveals its role as regulator of synaptic plasticity
527   and cognitive function. *Proc Natl Acad Sci U S A* **110**, 6583-6588
528   (2013).
529   40.   M. E. Schwab, Functions of Nogo proteins and their receptors in the
530   nervous system. *Nat Rev Neurosci* **11**, 799-811 (2010).
531   41.   Y. Fan, X. Tang, E. Vitriol, G. Chen, J. Q. Zheng, Actin capping protein
532   is required for dendritic spine development and synapse formation. *J*
533   *Neurosci* **31**, 10228-10233 (2011).
534   42.   T. Kitanishi *et al.*, Activity-dependent localization in spines of the F-
535   actin capping protein CapZ screened in a rat model of dementia.
536   *Genes Cells* **15**, 737-747 (2010).
537   43.   G. G. Farias, C. M. Guardia, R. De Pace, D. J. Britt, J. S. Bonifacino,
538   BORC/kinesin-1 ensemble drives polarized transport of lysosomes into
539   the axon. *Proc Natl Acad Sci U S A* **114**, E2955-E2964 (2017).
540   44.   I. H. Kim, H. Wang, S. H. Soderling, R. Yasuda, Loss of Cdc42 leads to
541   defects in synaptic plasticity and remote memory recall. *Elife* **3**, (2014).
542   45.   P. W. Beesley, R. Herrera-Molina, K. H. Smalla, C. Seidenbecher, The
543   Neuroplastin adhesion molecules: key regulators of neuronal plasticity
544   and synaptic function. *J Neurochem* **131**, 268-283 (2014).
545   46.   R. Herrera-Molina *et al.*, Neuroplastin deletion in glutamatergic neurons
546   impairs selective brain functions and calcium regulation: implication for
547   cognitive deterioration. *Sci Rep* **7**, 7273 (2017).

548 47. N. Schmidt *et al.*, Neuroplastin and Basigin Are Essential Auxiliary
549   Subunits of Plasma Membrane Ca(2+)-ATPases and Key Regulators of
550   Ca(2+) Clearance. *Neuron* **96**, 827-838 e829 (2017).
551 48. M. S. Lowenthal, S. P. Markey, A. Dosemeci, Quantitative mass
552   spectrometry measurements reveal stoichiometry of principal
553   postsynaptic density proteins. *J Proteome Res* **14**, 2528-2538 (2015).
554 49. K. N. Richter *et al.*, Comparative synaptosome imaging: a semi-
555   quantitative method to obtain copy numbers for synaptic and neuronal
556   proteins. *Sci Rep* **8**, 14838 (2018).
557 50. M. Sheng, E. Kim, The postsynaptic organization of synapses. *Cold
558   Spring Harb Perspect Biol* **3**, (2011).
559 51. B. G. Wilhelm *et al.*, Composition of isolated synaptic boutons reveals
560   the amounts of vesicle trafficking proteins. *Science* **344**, 1023-1028
561   (2014).
562 52. N. Nagaraj *et al.*, Deep proteome and transcriptome mapping of a
563   human cancer cell line. *Mol Syst Biol* **7**, 548 (2011).
564 53. B. Schwanhausser *et al.*, Global quantification of mammalian gene
565   expression control. *Nature* **473**, 337-342 (2011).
566 54. K. M. Harris, R. J. Weinberg, Ultrastructure of synapses in the
567   mammalian brain. *Cold Spring Harb Perspect Biol* **4**, (2012).
568 55. K. S. Kosik, Life at Low Copy Number: How Dendrites Manage with So
569   Few mRNAs. *Neuron* **92**, 1168-1180 (2016).
570 56. T. Shigeoka *et al.*, Dynamic Axonal Translation in Developing and
571   Mature Visual Circuits. *Cell* **166**, 181-192 (2016).
572 57. T. J. Younts *et al.*, Presynaptic Protein Synthesis Is Required for Long-
573   Term Plasticity of GABA Release. *Neuron* **92**, 479-492 (2016).
574 58. J. N. Bourne, K. E. Sorra, J. Hurlburt, K. M. Harris, Polyribosomes are
575   increased in spines of CA1 dendrites 2 h after the induction of LTP in
576   mature rat hippocampal slices. *Hippocampus* **17**, 1-4 (2007).
577 59. V. Tatavarty *et al.*, Single-molecule imaging of translational output from
578   individual RNA granules in neurons. *Mol Biol Cell* **23**, 918-929 (2012).
579 60. K. M. Harris, J. K. Stevens, Dendritic spines of CA 1 pyramidal cells in
580   the rat hippocampus: serial electron microscopy with reference to their
581   biophysical characteristics. *J Neurosci* **9**, 2982-2997 (1989).
582 61. C. Wang, B. Han, R. Zhou, X. Zhuang, Real-Time Imaging of
583   Translation on Single mRNA Transcripts in Live Cells. *Cell* **165**, 990-
584   1001 (2016).
585 62. D. Panja *et al.*, Two-stage translational control of dentate gyrus LTP
586   consolidation is mediated by sustained BDNF-TrkB signaling to MNK.
587   *Cell Rep* **9**, 1430-1445 (2014).
588 63. G. M. Schratt, E. A. Nigh, W. G. Chen, L. Hu, M. E. Greenberg, BDNF
589   regulates the translation of a select group of mRNAs by a mammalian
590   target of rapamycin-phosphatidylinositol 3-kinase-dependent pathway
591   during neuronal development. *J Neurosci* **24**, 7366-7377 (2004).
592 64. W. S. Sossin, M. Costa-Mattioli, Translational Control in the Brain in
593   Health and Disease. *Cold Spring Harb Perspect Biol*, (2018).
594 65. L. Ciandrini, I. Stansfield, M. C. Romano, Ribosome traffic on mRNAs
595   maps to gene ontology: genome-wide quantification of translation

596   initiation rates and polysome size regulation. *PLoS Comput Biol* **9**,
597   e1002866 (2013).

598 66.   S. Das Sharma *et al.*, Widespread Alterations in Translation Elongation
599   in the Brain of Juvenile Fmr1 Knockout Mice. *Cell Rep* **26**, 3313-3322
600   e3315 (2019).

601 67.   L. D. Fernandes, A. P. S. Moura, L. Ciandrini, Gene length as a
602   regulator for ribosome recruitment and protein synthesis: theoretical
603   insights. *Sci Rep* **7**, 17409 (2017).

604 68.   B. Schwanhausser *et al.*, Corrigendum: Global quantification of
605   mammalian gene expression control. *Nature* **495**, 126-127 (2013).

606 69.   M. K. Thompson, M. F. Rojas-Duran, P. Gangaramani, W. V. Gilbert,
607   The ribosomal protein Asc1/RACK1 is required for efficient translation
608   of short mRNAs. *Elife* **5**, (2016).

609 70.   D. E. Weinberg *et al.*, Improved Ribosome-Footprint and mRNA
610   Measurements Provide Insights into Dynamics and Regulation of Yeast
611   Translation. *Cell Rep* **14**, 1787-1799 (2016).

612 71.   K. Leppek, R. Das, M. Barna, Functional 5' UTR mRNA structures in
613   eukaryotic translation regulation and how to find them. *Nat Rev Mol*
614   *Cell Biol* **19**, 158-174 (2018).

615 72.   C. Mayr, Regulation by 3'-Untranslated Regions. *Annu Rev Genet* **51**,
616   171-194 (2017).

617 73.   D. Balchin, M. Hayer-Hartl, F. U. Hartl, In vivo aspects of protein folding
618   and quality control. *Science* **353**, aac4354 (2016).

619 74.   J. Zhao, B. Qin, R. Nikolay, C. M. T. Spahn, G. Zhang, Translatomics:
620   The Global View of Translation. *Int J Mol Sci* **20**, (2019).

621 75.   J. M. Taliaferro *et al.*, Distal Alternative Last Exons Localize mRNAs to
622   Neural Projections. *Mol Cell* **61**, 821-833 (2016).

623 76.   C. Andreassi *et al.*, An NGF-responsive element targets myo-inositol
624   monophosphatase-1 mRNA to sympathetic neuron axons. *Nat*
625   *Neurosci* **13**, 291-301 (2010).

626 77.   C. Giorgi *et al.*, The EJC factor eIF4AIII modulates synaptic strength
627   and neuronal protein expression. *Cell* **130**, 179-191 (2007).

628 78.   J. C. Darnell, J. D. Richter, Cytoplasmic RNA-binding proteins and the
629   control of complex brain function. *Cold Spring Harb Perspect Biol* **4**,
630   a012344 (2012).

631 79.   A. Zappulo *et al.*, RNA localization is a key determinant of neurite-
632   enriched proteome. *Nat Commun* **8**, 583 (2017).

633 80.   S. Sambandan *et al.*, Activity-dependent spatially localized miRNA
634   maturation in neuronal dendrites. *Science* **355**, 634-637 (2017).

635 81.   K. T. Thomas, C. Gross, G. J. Bassell, microRNAs Sculpt Neuronal
636   Communication in a Tight Balance That Is Lost in Neurological
637   Disease. *Front Mol Neurosci* **11**, 455 (2018).

638 82.   T. Udagawa *et al.*, Bidirectional control of mRNA translation and
639   synaptic plasticity by the cytoplasmic polyadenylation complex. *Mol*
640   *Cell* **47**, 253-266 (2012).

641 83.   J. D. Richter, J. Coller, Pausing on Polyribosomes: Make Way for
642   Elongation in Translational Control. *Cell* **163**, 292-300 (2015).

643 84. E. Santini, T. N. Huynh, E. Klann, Mechanisms of translation control
644   underlying long-lasting synaptic plasticity and the consolidation of long-
645   term memory. *Prog Mol Biol Transl Sci* **122**, 131-167 (2014).
646 85. N. R. Genuth, M. Barna, The Discovery of Ribosome Heterogeneity
647   and Its Implications for Gene Regulation and Organismal Life. *Mol Cell*
648   **71**, 364-374 (2018).
649 86. J. C. Darnell *et al.*, FMRP stalls ribosomal translocation on mRNAs
650   linked to synaptic function and autism. *Cell* **146**, 247-261 (2011).
651 87. E. Chen, M. R. Sharma, X. Shi, R. K. Agrawal, S. Joseph, Fragile X
652   mental retardation protein regulates translation by binding directly to
653   the ribosome. *Mol Cell* **54**, 407-417 (2014).
654 88. R. S. Muddashetty *et al.*, Reversible inhibition of PSD-95 mRNA
655   translation by miR-125a, FMRP phosphorylation, and mGluR signaling.
656   *Mol Cell* **42**, 673-688 (2011).
657 89. M. A. Sutton, A. M. Taylor, H. T. Ito, A. Pham, E. M. Schuman,
658   Postsynaptic decoding of neural activity: eEF2 as a biochemical sensor
659   coupling miniature synaptic transmission to local protein synthesis.
660   *Neuron* **55**, 648-661 (2007).
661 90. L. Ceolin *et al.*, Cell Type-Specific mRNA Dysregulation in
662   Hippocampal CA1 Pyramidal Neurons of the Fragile X Syndrome
663   Mouse Model. *Front Mol Neurosci* **10**, 340 (2017).
664 91. G. Aakalu, W. B. Smith, N. Nguyen, C. Jiang, E. M. Schuman, Dynamic
665   visualization of local protein synthesis in hippocampal neurons. *Neuron*
666   **30**, 489-502 (2001).
667 92. E. Puighermanal *et al.*, Anatomical and molecular characterization of
668   dopamine D1 receptor-expressing neurons of the mouse CA1 dorsal
669   hippocampus. *Brain Struct Funct* **222**, 1897-1911 (2017).
670 93. P. Bernabo *et al.*, In Vivo Translatome Profiling in Spinal Muscular
671   Atrophy Reveals a Role for SMN Protein in Ribosome Biology. *Cell*
672   *Rep* **21**, 953-965 (2017).
673 94. W. P. Lou, A. Baser, S. Klussmann, A. Martin-Villalba, In vivo
674   interrogation of central nervous system translatome by polyribosome
675   fractionation. *J Vis Exp*, (2014).
676 95. N. J. McGlincy, N. T. Ingolia, Transcriptome-wide measurement of
677   translation by ribosome profiling. *Methods* **126**, 112-129 (2017).
678 96. N. T. Ingolia, G. A. Brar, S. Rouskin, A. M. McGeachy, J. S. Weissman,
679   The ribosome profiling strategy for monitoring translation in vivo by
680   deep sequencing of ribosome-protected mRNA fragments. *Nat Protoc*
681   **7**, 1534-1550 (2012).
682 97. J. R. Wisniewski, A. Zougman, N. Nagaraj, M. Mann, Universal sample
683   preparation method for proteome analysis. *Nat Methods* **6**, 359-362
684   (2009).
685 98. A. Bastide, J. W. Yewdell, A. David, The RiboPuromycylation Method
686   (RPM): an Immunofluorescence Technique to Map Translation Sites at
687   the Sub-cellular Level. *Bio Protoc* **8**, (2018).
688 99. A. Biever *et al.*, PKA-dependent phosphorylation of ribosomal protein
689   S6 does not correlate with translation efficiency in striatonigral and

690 striatopallidal medium-sized spiny neurons. *J Neurosci* **35**, 4113-4130
691 (2015).
692 100. J. Cox, M. Mann, MaxQuant enables high peptide identification rates,
693 individualized p.p.b.-range mass accuracies and proteome-wide protein
694 quantification. *Nat Biotechnol* **26**, 1367-1372 (2008).
695 101. J. A. Vizcaino *et al.*, 2016 update of the PRIDE database and its
696 related tools. *Nucleic Acids Res* **44**, D447-456 (2016).
697 102. S. Tyanova *et al.*, The Perseus computational platform for
698 comprehensive analysis of (prote)omics data. *Nat Methods* **13**, 731-
699 740 (2016).
700 103. M. Martin, Cutadapt removes adapter sequences from high-throughput
701 sequencing reads. *EMBnet.journal17.1*, (2011).
702 104. B. Langmead, S. L. Salzberg, Fast gapped-read alignment with Bowtie
703 2. *Nat Methods* **9**, 357-359 (2012).
704 105. A. Dobin *et al.*, STAR: ultrafast universal RNA-seq aligner.
705 *Bioinformatics* **29**, 15-21 (2013).
706 106. D. Karolchik *et al.*, The UCSC Table Browser data retrieval tool.
707 *Nucleic Acids Res* **32**, D493-496 (2004).
708 107. A. R. Quinlan, I. M. Hall, BEDTools: a flexible suite of utilities for
709 comparing genomic features. *Bioinformatics* **26**, 841-842 (2010).
710 108. Y. Liao, G. K. Smyth, W. Shi, featureCounts: an efficient general
711 purpose program for assigning sequence reads to genomic features.
712 *Bioinformatics* **30**, 923-930 (2014).
713 109. J. M. Rodriguez *et al.*, APPRIS 2017: principal isoforms for multiple
714 gene sets. *Nucleic Acids Res* **46**, D213-D217 (2018).
715 110. A. Zhu, J. G. Ibrahim, M. I. Love, Heavy-tailed prior distributions for
716 sequence count data: removing the noise and preserving large
717 differences. *Bioinformatics* **35**, 2084-2092 (2019).
718 111. J. Cox, M. Mann, 1D and 2D annotation enrichment: a statistical
719 method integrating quantitative proteomics with complementary high-
720 throughput data. *BMC Bioinformatics* **13 Suppl 16**, S12 (2012).
721 112. W. J. Kent *et al.*, The human genome browser at UCSC. *Genome Res*
722 **12**, 996-1006 (2002).
723 113. G. Yu, L. G. Wang, Y. Han, Q. Y. He, clusterProfiler: an R package for
724 comparing biological themes among gene clusters. *OMICS* **16**, 284-
725 287 (2012).
726 114. R. Lorenz *et al.*, ViennaRNA Package 2.0. *Algorithms Mol Biol* **6**, 26
727 (2011).
728 115. E. Trotta, On the normalization of the minimum free energy of RNAs by
729 sequence length. *PLoS One* **9**, e113380 (2014).
730 116. R. Jansen, H. J. Bussemaker, M. Gerstein, Revisiting the codon
731 adaptation index from a whole-genome perspective: analyzing the
732 relationship between gene expression and codon occurrence in yeast
733 using a variety of models. *Nucleic Acids Res* **31**, 2242-2251 (2003).
734 117. A. K. Sharma *et al.*, A chemical kinetic basis for measuring translation
735 initiation and elongation rates from ribosome profiling data. *PLoS*
736 *Comput Biol* **15**, e1007070 (2019).

737   118. M. Torrisi, M. Kaleel, G. Pollastri, Deeper Profiles and Cascaded
738   Recurrent and Convolutional Neural Networks for state-of-the-art
739   Protein Secondary Structure Prediction. *Sci Rep* **9**, 12374 (2019).
740   119. P. Jones *et al.*, InterProScan 5: genome-scale protein function
741   classification. *Bioinformatics* **30**, 1236-1240 (2014).
742

768   **List of supplementary materials:**
769   Materials and Methods
770   Fig. S1-S16
771   Table S1
772   References (90-119)
773

774   **Fig. 1. Monosomes are the major ribosome population in neuronal**
775   **processes. (A)** Immunofluorescence labeling of the nascent protein metabolic
776   label (cyan) and the *Cornu Ammonis* 1 (CA1) pyramidal neuron marker Wfs1
777   (purple) in hippocampal sections from mice that received a brief infusion of
778   puromycin without (left) or with the protein synthesis inhibitor anisomycin (right)
779   into the lateral ventricle. Scale bar = 20 *µm*. A higher magnification image of
780   the nascent protein signal in the boxed dendritic region is shown. Scale bar =
781   50 *µm*. so, *stratum oriens*; sp, *stratum pyramidale*; sr, *stratum radiatum,* slm,
782   *stratum lacunosum moleculare*. **(B)** Scheme of a hippocampal slice showing
783   the regions (somata and neuropil) that were microdissected for subsequent
784   polysome profiling. Representative polysome profiles **(C and D)** and

comparison of the monosome:polysome (M/P) ratios **(E)** of the microdissected somata (blue; M/P= 0.30±0.03) or neuropil (purple; M/P= 0.76±0.19) (n= 7 biological replicates). Areas measured to calculate the M/P ratios are shaded (see methods). *** $p \leq 0.001$, Welch's t-test. **(F)** Scheme showing DIV 21 cortical neurons grown on a microporous membrane enabling the separation of cell bodies and neurites for polysome profiling. Representative polysome profiles **(G and H)** and M/P ratios **(I)** of the cell body (blue) or neurite layer (purple) (n= 4). Areas measured to calculate the Mono/Poly ratios are shaded. * $p \leq 0.05$, Welch's t-test.

Fig. 2. Neuronal monosomes actively elongate transcripts in the neuropil. **(A)** Experimental workflow. Somata or neuropil fractions were obtained, mono-/polysomes were isolated by polysome profiling and then ribosome profiling was performed on isolated fractions. **(B and C)** Metagene analyses showing the footprint density throughout the transcript open reading frame in the neuropil monosomes **(B)** or polysomes **(C)**. The average relative normalized coverage is plotted per nucleotide position, and the standard deviation is shaded (n= 3). Genes were individually normalized. **(D)** To assess the translational status of neuronal monosomes or polysomes, only reads classified as excitatory neuron-specific (see fig. S5) were retained for further analysis. **(E)** Metagene analyses showing the P-site coverage of neuronal transcripts in the neuropil monosome sample. The average normalized coverage is plotted per nucleotide position around the 5' end (start), central portion (center) and 3'end (stop) of the ORF. The standard deviation is shaded (n= 3).

Fig. 3. Local translation of key synaptic transcripts is predominantly accomplished by monosomes. (A) MA plot (the average, A, of the log read counts versus the differences in the log read counts, minus, M) showing transcripts with significantly enriched monosome (cyan) or polysome (orange) footprint coverage in the central portion of the ORF (region spanning 15 codons from the start site to 5 codons before the stop site). DESeq2, with a threshold of 0.05 on the adjusted p-value; see Methods. **(B to D)** Genome browser views representing the average monosome (top) or polysome (bottom) footprint coverage for 3 transcripts: *Kif1a* **(B)**, *Camk2a* **(C)** and *Slc17a7* **(D)**. Y axis indicates the number of normalized reads. **(E)** Metagene analysis showing the monosome P-site coverage of transcripts that exhibit significant monosome enrichment in the neuropil. The average normalized coverage is plotted per nucleotide position around the 5' end (start), central portion (center) and 3'end (stop) of the ORF. The standard deviation is shaded (n= 3). Inset shows the observed (obs) to expected (exp) ratio of the footprint distribution in different reading frames. $p = 2.26e-04$, ANOVA. **(F)** A pause score was computed for each codon located in the elongating ORF portion of the 463 monosome-enriched transcripts: pause score (z-score) = (normalized footprint coverage in monosome library − normalized footprint coverage in polysome library) / (normalized footprint coverage in polysome library)$^{1/2}$(n= 3). Fraction of codons per pause score. Dashed lines highlight pause score values of -/+ 1.96 ($p =$ 0.05), values between these lines represent codons exhibiting similar coverage in monosome and polysome libraries. **(G)** GO terms representing the top ten

833 significantly enriched protein function groups for monosome (cyan) or polysome
834 (orange)-enriched transcripts. **(H)** Scheme of pre- and post-synaptic
835 compartments highlighting some of the transcripts preferentially translated by
836 monosomes (cyan) or polysomes (orange). Key synaptic components that were
837 manually added owing to their exclusion by the excitatory neuron-specific filter
838 are represented with an asterisk. (See Table S1 for information about the fold-
839 changes).
840
841 **Fig. 4. Localization influences the translational status of selective**
842 **transcripts. (A)** Monosome to polysome $\log_2$ fold-changes (FC) in the neuropil
843 (y-axis) versus the somata (x-axis). The majority of transcripts exhibited
844 correlated (R^2= 0.6, p < 2.2e-16) monosome:polysome enrichments between
845 both compartments. Colored dots highlight transcripts that exhibit significantly
846 increased (cyan, n= 136) or decreased (purple, n= 36) monosome:polysome
847 $\log_2$ fold-changes in the neuropil compared to the somata. DESeq2, with a
848 threshold of 0.05 on the adjusted p-value; see Methods. Numbers represent the
849 different quadrants. **(B and C)** Example (*Arc*) **(B)** and cumulative distribution
850 frequency of the monosome:polysome $\log_2$ fold-changes **(C)** of transcripts
851 exhibiting significantly higher monosome:polysome ratios in the somata
852 (purple) compared to the neuropil (dark purple). p = 6.128-05, Kolmogorov-
853 Smirnov-Test. **(D and E)** Example (*Serpini1*) **(D)** and cumulative distribution
854 frequency of the monosome: polysome $\log_2$ fold-changes **(E)** of transcripts
855 exhibiting significantly higher monosome:polysome ratios in the neuropil (dark
856 cyan) compared to the somata (cyan). p = 9.215-15, Kolmogorov-Smirnov-Test.
857 **(F)** Cumulative distribution frequency depicting the monosome:polysome $\log_2$
858 fold-changes of all genes (Fig.4A; cyan, purple and gray dots) in the somata
859 (red) and neuropil (black) indicating an overall tendency towards higher
860 monosome:polysome ratios in the neuropil. p = 1.692-08, Kolmogorov-
861 Smirnov-Test.
862
863 **Fig. 5. Monosome-preferring transcripts often encode abundant synaptic**
864 **proteins. (A and B)** Monosome:polysome fold-changes in the neuropil were
865 not correlated with the copy numbers of some key pre-synaptic (*51*) **(A)** and
866 post-synaptic proteins (*48*) **(B)**. Regression lines and corresponding adjusted
867 R^2 are represented (pre-synapse p = 0.1488, post-synapse p = 0.07145). **(C)**
868 Box plots of protein ($\log_2$iBAQ) measurements in the neuropil for monosome-
869 (mono, cyan) or polysome- (poly, orange) enriched genes. p = 2.735e-06,
870 Wilcoxon rank-sum test. Of 463 and 372 monosome-and polysome-preferring
871 transcripts in the neuropil, 326 and 242, respectively, passed the stringent
872 proteomics filtering criteria (see Methods). **(D)** A scatter plot of the protein
873 abundance ($\log_2$iBAQ) versus monosome:polysome fold-changes for
874 monosome (cyan)-, polysome (orange) -and non-enriched (gray) genes (R^2 =
875 0.021, p = 2.944e-11). The dashed line indicates the mean $\log_2$ iBAQ value.
876 Monosome-preferring transcripts encoding proteins with abundances greater
877 than average are highlighted by dark cyan dots (mono-high). **(E and F)** The
878 local proteome correlates with the local transcriptome and translatome. A
879 scatter plot of the protein abundance ($\log_2$iBAQ) versus RNA ($\log_2$TPM) (R^2 =
880 0.26, p < 2.2e-16) **(E)** and translation rate (obtained from total footprints, without

881   biochemical fractionation) ($R^2 = 0.33$, $p < 2.2e\text{-}16$) (**F**) measurements for all
882   genes. Monosome-preferring genes encoding high-abundance proteins are
883   highlighted by dark cyan dots.

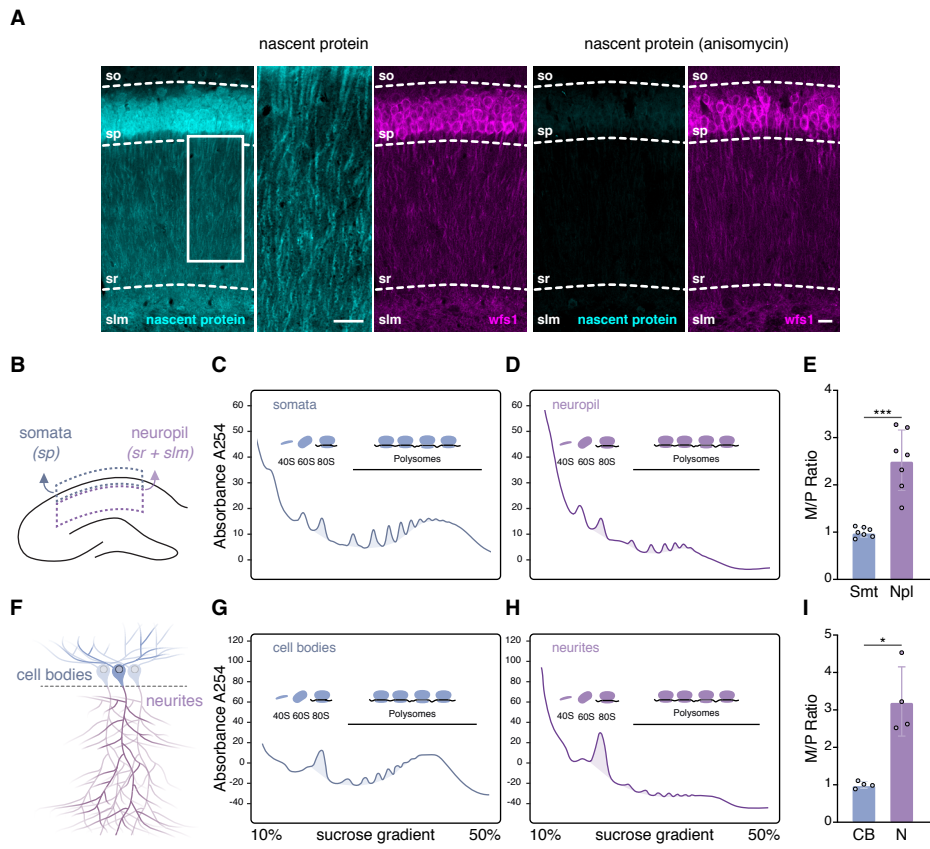# Figure 1. Monosomes are the major ribosome population in neuronal processes

A

nascent protein

nascent protein (anisomycin)

so
sp

sr

slm nascent protein | slm wfs1 | slm nascent protein | slm wfs1

B

somata *(sp)*   neuropil *(sr + slm)*

C somata

Absorbance A254

40S 60S 80S   Polysomes

D neuropil

Absorbance A254

40S 60S 80S   Polysomes

E

M/P Ratio

***

Smt   Npl

F

cell bodies   neurites

G cell bodies

Absorbance A254

40S 60S 80S   Polysomes

10%   sucrose gradient   50%

H neurites

40S 60S 80S   Polysomes

10%   sucrose gradient   50%

I

M/P Ratio

*

CB   N

Figure 2. Neuronal monosomes actively elongate transcripts in the neuropil

A

neuropil/somata
microdissection

↓

fractionation of monosomes
and polysomes

↓

+RNase

monosome
footprinting

polysome
footprinting

B

neuropil monosomes

relative coverage

-0.2 start 0.2 0.4 0.6 0.8 stop 1.2

relative position

C

neuropil polysomes

relative coverage

-0.2 start 0.2 0.4 0.6 0.8 stop 1.2

relative position

D

footprints

monosomes   polysomes

↓

alignment

↓

neuronal filter from
RiboTag (fig. S5)

↓

5' leader   coding region   3' UTR
       start   stop

E

normalized p-site coverage

neuronal neuropil monosomes

-25 start 25 50 75 -50 -25 center 25 50 -75 -50 -25 stop 25

nucleotide position

Figure 3. Local translation of key synaptic transcripts is predominantly accomplished by monosomes
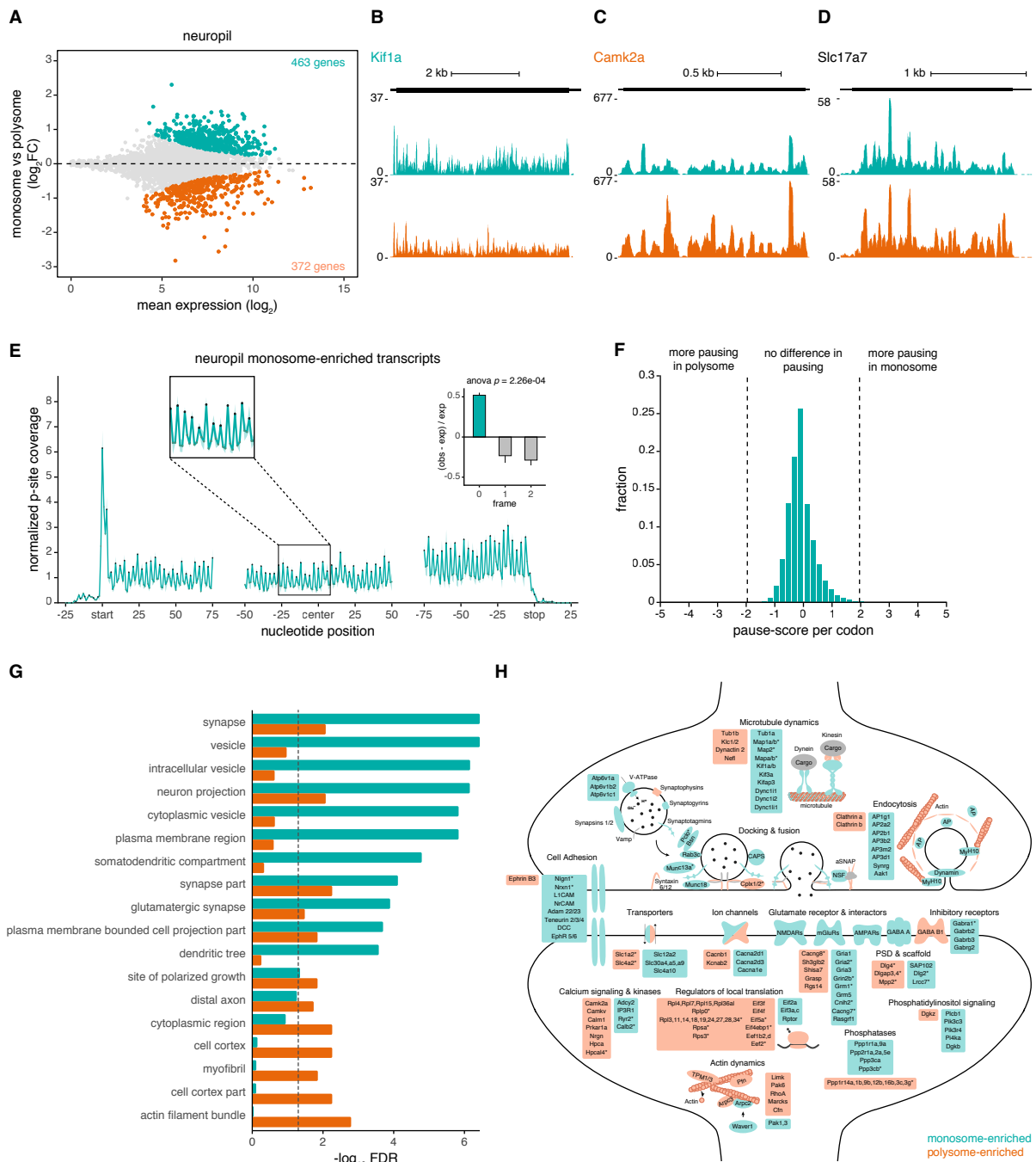
Figure 4. Localization influences the translational status of selective transcripts

A — mono:poly higher in neuropil / mono:poly higher in somata

monosome vs polysome (log₂FC) neuropil

II (npl mono / smt poly) | I (npl mono / smt mono)
III (npl poly / smt poly) | IV (npl poly / smt mono)

monosome vs polysome (log₂FC) somata

B — Arc, 1 kb

neuropil mono
neuropil poly
somata mono
somata poly

C — mono:poly higher in somata

ecdf

monosome vs polysome (log₂FC)

neuropil
somata
n = 36
p = 6.128e-05

D — Serpini1, 1 kb

neuropil mono
neuropil poly
somata mono
somata poly

E — mono:poly higher in neuropil

ecdf

monosome vs polysome (log₂FC)

neuropil
somata
n = 136
p = 9.215e-15

F — mono:poly overall

ecdf

monosome vs polysome (log₂FC)

neuropil
somata
p = 1.692e-08

Figure 5. Monosome-preferring transcripts often encode abundant synaptic proteins
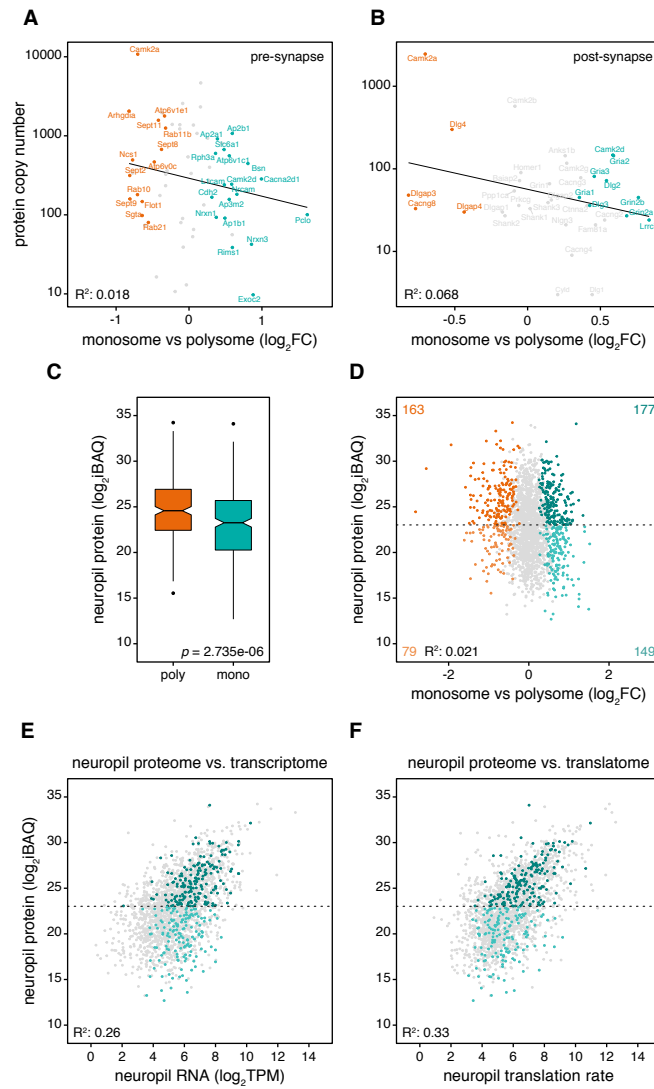
Supplementary Materials for

Title: Monosomes actively translate synaptic mRNAs in neuronal processes

Authors: Anne Biever[1†], Caspar Glock[1†], Georgi Tushev[1], Elena Ciirdaeva[1], Tamas Dalmay[1], Julian D. Langer[1,2], Erin M. Schuman[1*]

Affiliations:
[1]Max Planck Institute for Brain Research, Frankfurt, Germany
[2]Max Planck Institute of Biophysics, Frankfurt, Germany

[†] contributed equally
* to whom correspondence should be addressed:
erin.schuman@brain.mpg.de

This PDF includes:
Materials and Methods
Figs. S1 to S16

1 **Materials and Methods**

2 **1. Experimental Procedures**

3 **Animals**

4 Homozygous RiboTag Rpl22^HA/HA mice (The Jackson Laboratory, 011029)
5 were crossed with Camk2Cre (The Jackson Laboratory, 005359) or
6 Wfs1CreERT mice (The Jackson Laboratory, 009103). Male eight-week-old
7 C57Bl/6, Wfs1CreERT::RiboTag and Camk2Cre::RiboTag mice were housed
8 in standard cages and fed standard lab chow and water *ad libitum*. Male
9 Wfs1CreERT::RiboTag mice were treated for 3 days with tamoxifen (100
10 mg/kg, i.p., Sigma), dissolved in sunflower oil/ethanol (10:1) to a final
11 concentration of 10 mg/ml, and used 1 week later for immunostaining or
12 immunoprecipitation studies (*90*).
13 Adult male four-week-old Sprague Dawley SPF (Specific-Pathogen Free;
14 Charles River Laboratories) rats were housed on a 12/12 hour light dark cycle
15 with food and water *ad libitum* until sacrifice. Timed pregnant SPF (Charles
16 River Laboratories) females were housed in the institute's animal facility for
17 one week on a 12/12 hour light dark cycle with food and water *ad libitum* until
18 the litter was born. Cultured neurons were derived from P0 (postnatal day 0)
19 Sprague-Dawley rat pups (CD® Crl:CD, both male and female, RRID:
20 RGD_734476). Pups were sacrificed by decapitation.
21 The housing and sacrificing procedures involving animal treatment and care
22 were conducted in conformity with the institutional guidelines that are in
23 compliance with national and international laws and policies (DIRECTIVE
24 2010/63/EU; German animal welfare law; FELASA guidelines). The animals
25 were euthanized according to annex 2 of § 2 Abs. 2 Tierschutz-Versuchstier-
26 Verordnung. Animal numbers were reported to the local authority
27 (Regierungspräsidium Darmstadt, approval numbers: V54-19c20/15-
28 F126/1020 and V54-19c20/15-F126/1023).
29

30 **Hippocampal tissue collection and microdissection**
31 After sacrifice, the heads of four-week-old male rats (for polysome / ribosome
32 profiling experiments) or eight-week-old male mice (for translating ribosome
33 immunoprecipitation -RiboTag- experiments) were immediately immersed in
34 liquid nitrogen for 6sec to cool down the brains. The brains were removed, the
35 hippocampi were rapidly dissected on an ice-cooled disk. Hippocampal slices
36 (500 μm) were prepared in a drop of ice-cold RNase-free PBS containing 100
37 μg/ml cycloheximide using a manual tissue slicer (Stoelting). Each slice was
38 immediately passed to a second experimenter who microdissected the CA1
39 somatic and the neuropil layer at 0-4°C on a cold-plate (TCP50,
40 Thermoelectrics) in a drop of ice-cold RNase-free PBS containing 100 μg/ml
41 cycloheximide. To ensure the purity of the microdissected neuropil, only slices
42 located in the middle portion of the dorso-ventral axis of the hippocampus
43 were used (~ 6 slices per hippocampus). Somata and neuropil sections were
44 immediately snap-frozen after their dissection und kept at -80°C until lysis.
45
46

Primary hippocampal and cortical cultures
Dissociated rat hippocampal or cortical neurons were prepared from P0 day-old rat pups as previously described (*91*). For hippocampal cultures, neurons were plated at a density of 31.250 cells/ cm^2 onto 100 mm culture dishes and cultured for 21 days *in vitro* (DIV) in pre-conditioned growth medium (Neurobasal-A supplemented with B27 and GlutaMAX, 30% glia-culture supernatant, 15% cortex-culture supernatant). Cortical neurons were plated at a density of 100.000 cells/cm² onto poly-d-lysine-coated 100 mm, 3 μm pore polycarbonate membrane culture inserts (Corning 3420). At one DIV, AraC was added at a final concentration of 5 μM. After 2 days, medium was exchanged to pre-conditioned growth medium and neurons were cultured until 21 DIV. All cultures were maintained in a humidified incubator at 37°C and 5% CO_2. The sex of animals from which the cells were obtained was not determined.

Run-off experiment in primary hippocampal culture
24 h before the drug treatment, cell medium was adjusted to 8 ml per dish. Harringtonine (LKT Laboratories) was added at a final concentration of 2 μg/μl from a 2 mg/ml stock in 100% ethanol. Cells were returned to the incubator at 37°C for 30 sec or 90 sec. Cycloheximide was added to a final concentration of 100 μg/ml from a stock of 50 mg/ml in 100% ethanol. Following drug addition, cells were returned in the incubator at 37°C for 1 min. After the incubation with cycloheximide, the cells were placed on ice immediately and washed twice with ice-cold PBS + 100 *µg*/ml cycloheximide and lysed in polysome lysis buffer as described below. Total footprint libraries were prepared as described below.

Immunolabeling of cortical neurons cultured on membrane inserts
At 21 DIV, a part of the membrane was excised, briefly submerged in PBS pH 7.5 and fixed for 20 min in PFA (4 % paraformaldehyde in PBS pH 7.5). Cells were permeabilized with 0.5% Triton X-100 in PBS pH 7.5 supplemented with 4% goat serum for 15 min and blocked with blocking buffer (4% goat serum in PBS pH 7.5) for 1h. Dendrites were stained using an anti-MAP2 antibody (SySy 188004, 1:1000) in blocking buffer overnight at 4°C. After washing the cells three times for 5 min in PBS pH 7.5, the secondary antibody (ThermoFisher A488 A-11073, 1:1000) was incubated in blocking buffer for 45 min at room temperature. Cells were washed three times for 5 min in PBS pH 7.5 with DAPI added to the second wash. Membranes were mounted on glass slides using Aqua Poly/Mount and imaged from the top (cell body fraction) or bottom (neurite fraction).

Tagged ribosome immunoprecipitation
HA-tagged ribosome immunoprecipitation of hippocampi from male Camk2Cre::RiboTag or somata/neuropil sections from male Wfs1Cre::RiboTag mice was performed as described previously (*18, 92*) with slight modifications. Tissue sections were homogenized in a glass homogenizer containing ice-cold RiboTag lysis buffer (50 mM Tris pH 7.4, 100 mM KCl, 12 mM $MgCl_2$, 1% NP40, 1 mM DTT, 20 U/ml SUPERaseIN*RNAse inhibitor (Ambion), 200 U/ml RNAsin (Promega), 100 μg/ml cycloheximide, 10

95　U/ml TurboDNAse, protease inhibitor (Roche)). After triturating the lysate 10
96　times using a 23 Gauge syringe, samples were chilled on ice for 10 min and
97　cleared by centrifugation at 16.100g for 10 min. Ten percent of the
98　supernatant were kept as an input. HA-immunoprecipitation (IP) was
99　performed by incubation of the remaining supernatant with 5 µl of anti-HA
100　antibody (abcam Ab9110) over night at 4°C with gentle rotation. Incubation of
101　the samples with magnetic beads (Dynabeads protein G, Invitrogen), washes
102　and elution were performed according to (*92*). Total RNA was extracted from
103　both the input and immunoprecipitated ribosome-mRNA complexes, using the
104　RNeasy MinElute kit (Qiagen). RNA integrity was assessed using the Agilent
105　RNA 6000 Pico kit.
106
107　**Lysate preparation for polysome and ribosome profiling**
108　*Tissue*
109　Rat tissue samples were homogenized in polysome lysis buffer (20 mM Tris
110　pH 7.5, 150 mM NaCl, 5 mM $MgCl_2$, 24 U/ml TurboDNAse, 100 µg/ml
111　cycloheximide, 1 mM DTT, 1% Triton X100 and protease inhibitor mixture
112　(Roche)) (*25*) by douncing in a glass homogenizer. For the experiments
113　including RNase inhibitors, the polysome lysis buffer was supplemented with
114　200U/ml RNase inhibitors (Promega). After triturating the lysate 10 times
115　using a 23 Gauge syringe, samples were chilled on ice for 10 min and cleared
116　by two centrifugations at 16,100g for 6 min.
117
118　*Neuronal Culture*
119　At 21 DIV rat cortical primary neurons were washed twice in ice-old PBS pH
120　7.5 supplemented with 100 µg/ml cycloheximide. Neurons were collected with
121　a scraper in polysome lysis buffer (20 mM Tris pH7.5, 150 mM NaCl, 5 mM
122　$MgCl_2$, 24 U/ml TurboDNAse, 100 µg/ml cycloheximide, 1 mM DTT, protease
123　inhibitor mixture (Roche) and 8% glycerol). After scraping, the lysates were
124　supplemented with Triton X100 to a final concentration of 1% and chilled on
125　ice for 10 min. After triturating the lysates 10 times using a 23 Gauge syringe,
126　samples were chilled on ice for 10 min and then cleared by centrifugation at
127　16,100g for 10 min.
128
129　**Polysome profiling**
130　Samples were loaded onto 6 ml 10-50% sucrose density gradients that were
131　prepared w/v in the following gradient buffer: 20 mM Tris pH 7.5, 150 mM
132　NaCl, 5 mM $MgCl_2$, 100 µg/ml cycloheximide, 1 mM DTT. For polysome
133　profiling from neuronal cultures, the gradient buffer was supplemented with
134　8% glycerol. To ensure proper RNase digestion during ribosome profiling on
135　the sucrose gradient fractions, RNase inhibitors were omitted from the
136　polysome lysis buffer. RNase-free reagents were used and samples were
137　handeled on ice during the entire procedure. The similarity of the neuropil
138　polysome profiles in the presence or absence of RNase inhibitors indicated
139　that this procedure did not affect RNA integrity (fig. S16). Gradients were
140　centrifuged for 2h 45 at 36.000 r.p.m at 4°C in a SW41 Ti swing-out rotor.
141　Polysome profiling was performed using a density gradient fractionation
142　system (Brandel) with upward displacement and continuous monitoring at 254

143 nm using a UA-6 detector. The area under the curve (AUC) of individual
144 absorbance peaks was quantified. A monosome to polysome ratio was
145 calculated by relating the monosome AUC to the sum of the AUCs of all
146 polysome peaks. Somata and neuropil polysome profiles loaded with an equal
147 amount of RNA were used for representation and the comparisons of the
148 monosome or polysome AUC separately between compartments. Fractions of
149 125 µl corresponding to the monosome or the polysome peaks were collected
150 and pooled.
151
152 **Monosome and polysome footprint isolation**
153 For the entire hippocampus monosome and polysome footprinting, 3
154 replicates, each comprising the hippocampi from three rats, yielding ~150 µg
155 RNA, were used. For the somata and neuropil monosome and polysome
156 footprinting, three replicates each comprising a pool of microdissected tissue
157 from 55 rats, yielding ~110 µg RNA, was used. For each replicate,
158 microdissected tissue was lysed as described above and aliquots containing
159 20 or 10 µg of RNA were retained for total ribosome footprinting and total
160 RNA sequencing, respectively. The remaining lysate was loaded onto 10-50%
161 sucrose gradients and centrifuged as described above. To prevent masking of
162 the ribosome peaks by myelin (*93, 94*), each replicate was loaded onto 2-3
163 gradients and monosome or polysome fractions from different gradients were
164 pooled after polysome profiling. A volume of monosome / polysome fraction
165 containing 10 µg (hippocampi) or 2-5 µg (somata / neuropil) of RNA was
166 diluted with gradient buffer and digested with 7.5 U/µg RNA of RNase I
167 (epicenter) rotating for 45 min at 24°C (a range of RNase I concentrations was
168 tested beforehand to optimize the digestion conditions; Table S1). Nuclease
169 digestion reactions were promptly cooled, spun and 10 µl
170 SUPERaseIN*RNase inhibitor was added. Samples were then layered onto a
171 34% sucrose cushion, prepared w/v in gradient buffer supplemented with 20
172 U/µl of SUPERaseIN*RNase inhibitor. 80S particles were pelleted by
173 centrifugation in a SW55Ti rotor for 3h 30 at 55,000 r.p.m at 4°C.
174
175 **Total ribosome footprint isolation**
176 Neuropil lysates from three biological replicates (see section 'monosome and
177 polysome footprint isolation') containing 20 µg of RNA were digested with
178 0.5 U/µg RNase I (epicenter) shaking for 45 min at 400 r.p.m at 24°C (*95*).
179 Nuclease digestion reactions were promptly cooled, spun and 10 µl
180 SUPERaseIN*RNase inhibitor was added. Samples were then layered onto a
181 34% sucrose cushion, prepared w/v in gradient buffer supplemented with
182 20 U/µl of SUPERaseIN*RNase inhibitor. 80S particles were pelleted by
183 centrifugation in a SW55Ti rotor for 3h 30 at 55,000 r.p.m at 4°C.
184
185 **Ribosome footprint library preparation**
186 Footprint libraries were prepared according to McGlincy and Ingolia (2017)
187 (*95*) with the following modifications: After RNA extraction from the ribosomal
188 pellet, ribosomal RNAs were depleted using the Ribo-Zero Magnetic Gold
189 Mammalian kit (Illumina), followed by footprint purification using the RNA
190 clean & concentrator-5 kit (Zymo). Footprint fragments were purified by PAGE

purification on a 15% TBE-Urea gel and fragments from 26-34 nts were isolated. After footprint de-phosphorylation and linker ligation, the ligation reaction was depleted of unligated linker by incubation with 0.5 µl of 5' Yeast deadenylase 10 U/µl (NEB) and 0.5 µl of RecJ exonuclease 10 U/ul (Epicentre) for 45 min at 30°C. In addition, ligation products were purified by PAGE purification on a 15% TBE-Urea gel. Reverse transcription was performed as described previously, with the following modification: the reverse transcription reaction was directly incubated with 2 µl of exonuclease I at 37°C for 1h followed by 15 min at 80°C. cDNA was gel purified by PAGE on a 15% TBE-Urea gel. After circularization, circDNA was submitted to an additional ribosomal RNA depletion using 14 custom biotinylated rat rRNA oligos (Table S1) according to (96). After amplification, the libraries were run on an 8% non-denaturing TBE gel, 160 bp products were isolated and characterized using the Agilent High Sensitivity DNA assay. Libraries were sequenced on an Illumina NextSeq500, using a single-end, 52 bp run.

RNA isolation and library preparation
RNA was isolated from tissue lysates using the Direct-zol RNA micro Prep kit (Zymo). RNA integrity was assessed using the Agilent RNA 6000 Nano kit. Rat neuropil total RNA sequencing libraries were prepared starting from ~200 ng total RNA using the TruSeq stranded total RNA library prep gold kit (Illumina). For the input/IP samples from Camk2Cre::RiboTag hippocampi or Wfs1Cre::RiboTag somata and neuropil, mRNA sequencing libraries were prepared starting from ~100 ng total RNA using the TruSeq stranded mRNA library prep kit (Illumina). Libraries were sequenced on an Illumina NextSeq500, using a single-end, 75 bp run.

rRNA to total RNA percentage
The RNA was isolated from rat somata and neuropil (n=4) as described above and measured using the Agilent RNA 6000 Nano kit. The ratio of rRNA to total RNA was obtained by summing the 18S rRNA and 28S rRNA percentage of total RNA calculated by the Agilent Bioanalyzer.

Immunoblotting and western blotting
Neurite and cell body layers were collected in ice-cold PBS, centrifuged and pellets were lysed in lysis buffer (1% (w/v) Triton X100, 0.5% (w/v) SDS in PBS) supplemented with TurboDNase (24 U/ml) at 70 C for 15 min. Lysates were cleared by centrifugation and stored at -80 C until use. Somata and neuropil lysates were prepared in polysome buffer. Lysates were resolved by SDS-PAGE in 4-12% Bis-Tris gels (Invitrogen) and analyzed by immunoblotting using far-red fluorescent dyes and a Licor Odyssey scanner (mouse anti-NeuN (1:1000, MAB377); rabbit anti-bActin (1:2000, ab8227); anti-mouse IR800 (1:5000, Licor); anti-rabbit IR680 (1:5000, Licor)). Protein levels in bands of interest were quantified using ImageJ (NIH). Western blot normalization was conducted according to the Revert Total Protein Stain (Licor) manufacturer's instructions.

Mass spectrometry data acquisition

Three replicates of rat neuropil were microdissected as described above. Tissue pieces were snap-frozen and kept at -80°C until lysis. Tissue pieces were lysed in 4% Chaps, 8M Urea, 0.2M Tris HCl, 1M NaCl. All samples were digested, reduced and alkylated based on a previously published FASP-protocol (*97*). Dried peptide pellets were stored at -20 °C until LC-MS/MS analysis. Proteolytic digests were analysed via Nano-LC-MS/MS on an Ultimate 3000 nanoUPLC (Thermo Fisher Scientific, Bremen) coupled to a Orbitrap Fusion Lumos (Thermo Fisher Scientific, Bremen).

After dissolving the dried peptides in 20 µl 0.1% FA in 5% acetonitrile, samples were separated using an Acclaim pepmap C18 column (50 cm x 75 µm, particle size 2 µm) after trapping on an Acclaim pepmap C18 pre-column (2 cm x 75 µm, particle size 3 µm). Trapping was performed for 6min with a flow rate of 6µl/min using a loading buffer (98/2 water/acetonitrile with 0.05% Triflouroacetic acid). Peptides were then eluted and separated on the analytical column at a flow rate of 300nl/min with the following gradient: from 4 to 33% B in 150 min, 33 to 48% B in 20 min, 48 to 90% B in 1 min, and constant 90% for 13 min (buffer A: 0.1% FA in water, buffer B 0.1% FA in 80/20 acetonitrile/water). All LC-MS-grade solvents were purchased from Honeywell/ Riedel del Häen.

Peptides eluting from the column were ionised online using a Nano Flex ESI-source and analysed with an Orbitrap Fusion Lumos mass spectrometer in data-dependent-mode. Survey scans were acquired over the mass range of 350-1400 m/z in the Orbitrap (maximum injection time 50s, AGC, automatic gain control, fixed at $2x10E5$ and R = 120K) and sequence information was acquired by a "Top-Speed" method with a fixed cycle time of 2s for the survey and following MS/MS-scans. MS/MS-scans were performed on the most abundant precursors exhibiting a charge state from 2 to 5 with an intensity minimum of $5x10E3$. Picked precursors were isolated in the quadrupole at 1.4 Da and fragmented using HCD at NCE (normalized collision energy) = 30%. For MS/MS an AGC of 10E4 and a maximum injection time of 300 sec was used. Resulting fragments were detected in the Ion Trap using the rapid scan mode. The dynamic exclusion was set to 30 sec with a mass tolerance of 10 ppm. All samples were measured in technical triplicates.

Intracerebroventricular puromycin administration

Mice (n=3 per group) were anesthetized with isoflurane (induction: 4%, maintenance: 2%) in oxygen-enriched air (Oxymat 3, Weinmann, Hamburg, Germany) and fixed in a stereotaxic frame (Kopf Instruments, Tujunga, USA). Core body temperature was maintained at 37.5 °C by a feed-back controlled heating pad (FHC, Bowdoinham, ME, USA). Analgesia was provided by local injection of ropivacain under the scalp (Naropin, AstraZeneca, Switzerland) and systemic injection of metamizol (100 mg/kg, i.p., Novalgin, Sanofi) and meloxicam (2 mg/kg, i.p., Metacam, Boehringer-Ingelheim, Ingelheim, Germany) (*72*). A stainless steel 26-gauge guide cannula (PlasticsOne, Roanoke, VA) was implanted vertically towards the right lateral ventricle (A/P –0.22 mm; M/L 1 mm; D/V –2 mm). Guide cannulas were fixed onto the skull with instant adhesive (Ultra Gel©, Henkel, Düsseldorf, Germany) and dental

cement (Paladur©, Heraeus, Hanau, Germany). An obturator was inserted into each guide cannula and remained in place until the drug infusion when it was removed and replaced with an injector that extended 0.5 mm beyond the tip of the guide cannula. After surgery recovery, 3 µl of puromycin solution (9 mg/ml, 10% DMSO/90% saline) or vehicle were infused for 1 min into the cannula through polyethylene tubing using an infusion pump (Stoelting) (*73*). The protein synthesis inhibitor control received an infusion of 3 µl of anisomycin (25 µg/µl, initially dissolved in 3N HCl and brought to pH 7.3 by addition of 3N NaOH) (*74, 75*). Thirty min after the anisomycin infusion, mice were infused with 3 µl of puromycin (9 mg/ml) supplemented with 75 µg anisomycin. After drug infusions, the tubing remained in place for 1 extra minute to ensure proper delivery of the solution. All mice were previously handled to ensure proper immobility during intracerebroventricular administration. 10 min after puromycin infusion, mice were transcardially perfused as described below.

Immunolabeling of hippocampal slices
After anesthesia with isoflurane, mice were rapidly euthanized and transcardially perfused for 1 min with PBS pH 7.5 followed by 2 min with 4% (w/v) paraformaldehyde in PBS pH 7.5. Brains were post-fixed over night in the same solution and stored at 4°C. 30 µm thick sections were cut with a vibratome (Leica) and stored at 4°C in PBS pH 7.5, until they were processed for immunofluorescence. Hippocampal sections were identified using a mouse brain atlas and sections comprising between –1.34 and –2.06 mm from bregma were included in the analysis. Hippocampal sections from Wfs1Cre::RiboTag and Camk2Cre::RiboTag mice were processed as follows: free-floating sections were rinsed three times for 10 min with PBS pH 7.5. After 15 min incubation in 0.2% (v/v) Triton X-100 in PBS pH 7.5, sections were rinsed in PBS pH 7.5 again and blocked for 1 h in a solution of 3% BSA in PBS pH 7.5. Finally, they were incubated for 72 h at 4°C in 1% BSA, 0.15% Triton X-100 with the anti-HA antibody (abcam Ab9110, 1:500). *In vivo* puromycylated brain slices were immunostained as described previously (*98, 99*). Briefly, sections were incubated for 20 min with coextraction buffer (50 mM Tris-HCl, pH 7.5, 5 mM MgCl$_2$, 25 mM KCl, protease inhibitor mixture (Roche) and 0.015% digitonin (Wako Chemicals)). After three rinses with PBS pH 7.5, sections were incubated for 72 h at 4°C with puromycin (Milipore MAB E343, 1:1000) and Wfs1 (Proteintech 11558-1-AP, 1:1000) antibodies in a solution containing 0.05% saponin, 10 mM glycine, and 5% fetal bovine serum in PBS pH 7.5. After primary antibody incubation, sections were rinsed three times for 10 min in PBS pH 7.5 and incubated overnight at 4°C with the secondary antibody (ThermoFisher A546 A-11030, A647 A-21245, 1:500). Sections were rinsed three times for 10 min in PBS pH 7.5 and mounted in Aqua-Poly/Mount.

2. Data Analyses

Proteomics data analysis

Raw data were processed using the Max Quant software version 1.6.2.2 (*100*).

MS/MS- spectra were searched against the UniprotKB-database from Rattus norvegicus (36080 entries, downloaded on 21/12/2017) and additionally against a database containing common mass spec contaminations using the probabilistic based algorithm from the Andromeda search engine. The set of stringent constraints allowed only peptides with full tryptic specificity allowing N-terminal cleavage to proline and up to 2 missed cleavages. Carbamidomethylation of cysteine was set as fixed modification. Oxidation of methionine and acetylation of the protein N-terminus were set as variable modifications. Minimum peptide length was set to 7 amino acids. The first search was performed with 20 ppm precursor tolerance for mass recalibration and the main search mass tolerance was set to 4.5ppm. The fragment mass tolerance was 0.5 Da and the "match between runs" option was enabled. Peptides and proteins were identified based on a 1% FDR with the use of a decoy strategy and only those protein groups which were identified with at least 1 unique peptide were used for further analysis.

All proteomic data associated with this manuscript have been uploaded to the PRIDE online repository (*101*).

Proteomics post processing

The Perseus package v1.6.2.2 (*102*) was used for further bioinformatic analysis of the resulting expression data from MaxQuant. Before further processing, decoy and contaminant database hits as well as proteins only identified using modified peptides ("identified by site") were excluded. Additionally, only those protein groups which were identified in at least 2 out of 3 technical replicates and in 2 out of 3 biological replicates were considered for further analysis.

Footprint genome and transcriptome alignment

Adapters were removed with Cutadapt v1.15 (*103*) (--cut 1 –minimum-length 22 –discard-untrimmed –overlap 3 –e 0.2). An extended UMI was constructed from the two random nucleotides from the RT primer and the five random nucleotides from the linker and added to the description line using a custom perl script. Trimmed reads that aligned to rat ncRNA were removed using Bowtie2 v2.3.4.3 (*104*) (--very-sensitive). Remaining reads were aligned to the rat genome (rn6) with the split-aware aligner STAR v2.6.1a (*105*) (--twopassMode Basic --twopass1readsN -1 --seedSearchStartLmax 15 --outSJfilterOverhangMin 15 8 8 8 --outFilterMismatchNoverReadLmax 0.1). When required, STAR --quantMode was used to retrieve transcript coordinates. Transcriptome alignments were used for all analyses, except for differential expression and genomic feature analysis. The STAR genome index was built using annotation downloaded from the UCSC table browser. PCR duplicates were suppressed using a custom Perl script and alignments flagged as secondary alignment were filtered out.

RNA genome alignment

Adapters and low quality nucleotides were removed with Cutadapt v1.15 (*103*) (--minimum-length 25 –nextseq-trim=20). Reads were aligned to the rat (rn6) or the mouse (mm10) genome with STAR v2.6.1a (*105*).

Assigning footprint reads to genomic features

Genomic feature coordinates (CDS, 3'UTR, 5'UTR, intron) were downloaded from the UCSC table browser as BED files (*106*). Bedtools v2.26.0 (*107*) was used to first convert BAM files into the BED format and second to identify reads overlapping with the individual features.

Counting and differential expression analysis

Monosome to polysome ratios

Counts per gene were calculated from reads mapped to the genome using featureCounts v1.6.3 (*108*). Only a single transcript isoform, with the highest possible APPRIS score (*109*), was considered per gene. Only footprint reads aligned to the central portion of the ORF, by convention 15 codons from the start until 5 codons before the stop codon, were counted (*95*). Raw counts were fed into DESeq2 (*19*) for differential expression analysis. LFC shrinkage was used to generate more accurate $\log_2$ fold-change estimates (*110*). In order to test if the monosome to polysome fold change differs across compartments, an interaction was added to the design formula. In this analysis unshrunken $\log_2$ fold-changes were used.

RiboTag IP to input ratios

Counts per gene were calculated from reads mapped to the genome using featureCounts v1.6.3 (*108*). All transcript isoforms were considered. Raw counts were fed into DESeq2 and LFC shrinkage was used.

Classification of neuronal genes

A classifier to identify excitatory neuron-enriched genes was developed. The union of genes with significantly enriched RiboTag-IP to input fold-changes (threshold of 0.05 on the adjusted *p*-value and a 30% enrichment) was formed from the three RiboTag experiments (Hippocampus Camk2Cre::RiboTag, somata/neuropil Wfsr1Cre::RiboTag).

Classification of non-sense mediated decay (NMD) targets

Genes with the Ensembl biotype annotation 'nonsense_mediated_decay' and 'retained_intron' were classified as possible NMD targets.

Translation rate calculations

The translation rate was computed from three biological replicates of neuropil total ribosome footprinting, as previously described in (*66*). In brief, the number of footprint reads in the gene's CDS was divided by its CDS length in kilobases. This value was then normalized to the total number of footprint reads mapping to any region of the gene. Only reads with a minimum of 10 raw reads in all footprint libraries were used for analysis.

Translational efficiency calculations

Translational efficiency was computed from three biological replicates of neuropil total ribosome footprinting. The translational efficiency of a gene was calculated as the ratio of normalized footprint reads (TPMs) to normalized RNA-seq reads (TPMs).

Integration of proteomic and transcriptomic data

Protein and RNA data were matched as described in (*111*). A protein centric view was taken. For each protein in the protein group the corresponding RNA measures in transcripts per million (TPM) or the corresponding translation rates were summed and the mean of the corresponding monosome to polysome $\log_2$ fold-change was determined. In a functional group at least half the genes had to be classified as 'neuronal' in order to pass the RiboTag filter. A functional group was determined as 'monosome-enriched or polysome-enriched' if more than half of its transcripts were classified as 'monosome-enriched or polysome-enriched'. In all other cases, the functional group was classified as 'non-enriched'.

Metagene analysis

Metagene plots represent the accumulated footprint coverage over the length-normalized ORF. The normalized footprint coverage was generated for each gene (footprint coverage divided by the average codon coverage). Edge positions were defined relative to the ORF start and stop codons and divided into 100 bins. Each gene contributed with its average normalized footprint coverage per bin.

Harringtonine depletion profile analysis

Open reading frame footprint coverages per gene were generated for each time point. Analysis was performed on well-translated genes with at least 0.1 reads per codon. Profiles were scaled by the average coverage between codons 400 and 450. Transcripts shorter than 460 codons were excluded from the analysis. For each time point, the metagene profiles were smoothed in 30 codon windows and normalized to the 0s time point.

3-nucleotide periodicity analysis

First, the P-site offset was defined for individual footprint lengths. For this, all reads spanning the ORF start were used and the most probable offset from the start and end of the read was defined for each length. Second, the P-site position per read was determined based on its length and the previously defined offset. All P-site positions were projected for 100 nucleotides around the ORF start, stop and center. The P-site coverage of each gene was normalized to its average footprint coverage. The nucleotide coverage at frame positions 0, 1 and 2 were assessed. To determine if the observed frame fraction differed from the expected frame fraction, a one-way analysis of variance (ANOVA) was performed. A significant p-value rejects the null-hypothesis that all frames exhibit the expected P-site coverage.

Genome browser track visualization

Footprint coverage was visualized as custom tracks on the UCSC Genome Browser (*112*). Footprint alignments were converted into BedGraph files (https://genome.ucsc.edu/goldenPath/help/bedgraph.html) using Bedtools v2.26.0.

Gene ontology analysis

GO enrichment of monosome- or polysome-preferring genes was performed using the R package clusterProfiler (*113*) with a Benjamini-Hochberg multiple testing adjustment and a false-discovery rate cut-off of 0.05, using all expressed genes in the neuropil as background. The simplify function with a cutoff of 0.7 was used to remove redundancy from enriched GO terms.

Correlation between the monosome to polysome fold-change and transcript attributes

DNA sequences were extracted from the rat (rn6) version genome. Only genes with valid values for all transcript attributes were used for analysis. The length of 3'- and 5'UTRs was set to a minimum of 10 nts.

GC content

The GC content was assessed by counting the number of G or C bases in the sequence and then dividing by the number of bases in the predicted 5'UTR, CDS or 3′ UTR.

Minimum free energy (MFE)

The ViennaRNA package version 2.0 with RNAfold was used to calculate the minimum free energy per 5'UTR or 3′ UTR sequence (*114*). A method described by Trotta et al._(*115*) was adapted to normalize minimum free energy units to the sequence length. The sequence length was restricted to a maximum of 500 nts in proximity to the start and stop codon.

Codon adaptation index (CAI)

CAI values in the neuropil were obtained for neuronal genes only, following the procedure described in (*116*).

Initiation rate

The initiation rate per gene was calculated based on the neuropil total ribosome footprint and RNA coverage as previously described in (*117*). In short, the initiation rate depends on the translational efficiency (defined as described above), CDS length, average time for a ribosome to traverse the CDS and the normalized ribosome occupancy in the initial 10 codons of the CDS. The average elongation rate was assumed to be 4 codons / second (*61*). A ξ value of 0.0084 was determined from the best fit line to the average ribosome density of a transcript (from polysome profiling) versus its translational efficiency (from ribosome profiling and RNA-seq).

Mean typical decoding rate (MTDR)

A per gene MTDR was calculated based on the neuropil total ribosome

527 footprint coverage as previously described in (*26*). In short, each amino acid
528 decoding time was defined as a convolution of an average decoding time (a
529 gaussian component with the parameters μ and σ) and a pausing decoding
530 time (an exponential component with the parameter λ). A model fitting
531 procedure was used to deconvolve the two distributions and identify the three
532 parameters per amino acid. The geometric mean of all average decoding
533 times (μ) was calculated to determine the per-gene MTDR.
534
535 **Upstream open reading frame (uORF)**
536 To identify transcripts containing uORFs, neuropil total ribosome footprint
537 libraries from three replicates were used. Only genes with annotated 5'UTRs
538 were considered. A string match algorithm was used to identify sequences
539 within annotated 5'UTRs that are flanked by a canonical in-frame start and
540 stop codon. Only sequences with a minimum length of 3 codons and at least
541 10 raw footprints in all three replicates were considered as uORFs.
542
543 **Prediction of protein secondary structure and protein domains**
544 Appris transcript isoforms were translated into amino acid sequences and
545 used to predict secondary structures and protein domains. Porter 5 was used
546 to predict protein secondary structures in 3 classes (α-helix, β-strand and coil)
547 (*118*). Spans of coils were defined as unstructured, whereas helices and
548 strands were defined as structured sequences. Transitions from structured to
549 unstructured, and vice versa, were counted and normalized to the sequence
550 length. Protein domains were predicted using InterProScan5 based on the
551 Pfam database (*119*). Functional domains per protein were merged into
552 unique regions and their average length was compared between monosome-
553 and polysome-enriched genes.
554
555 **Codon pause score analysis**
556 For each codon in neuropil monosome-enriched genes (CDS only), a pause
557 score was calculated based on a z-score-like quantity: pause score =
558 (normalized footprint coverage in monosome library – normalized footprint
559 coverage in polysome library) / (normalized footprint coverage in polysome
560 library)$^{1/2}$. The resulting distribution represents the number of codons per
561 gene with different coverage (i.e. a measure of observed pausing).
562
563 **Ribotools**
564 All tools used in this study are contained in one modular C++ program called
565 ribotools. It relies on the HTSlib (https://github.com/samtools/htslib) for
566 parsing BAM files. The source code and further notes on the algorithms can
567 be found on our GitLab repository:
568 https://gitlab.mpcdf.mpg.de/mpibr/schu/ribotools
569
570 **Data and software availability**
571 The accession number for the raw sequencing data reported in this paper is:
572 NCBI BioProject: PRJNA550323
573 All proteomics data associated with this manuscript have been uploaded to
574 the PRIDE online repository.

575   Processed data used in this study are included as Table S1.
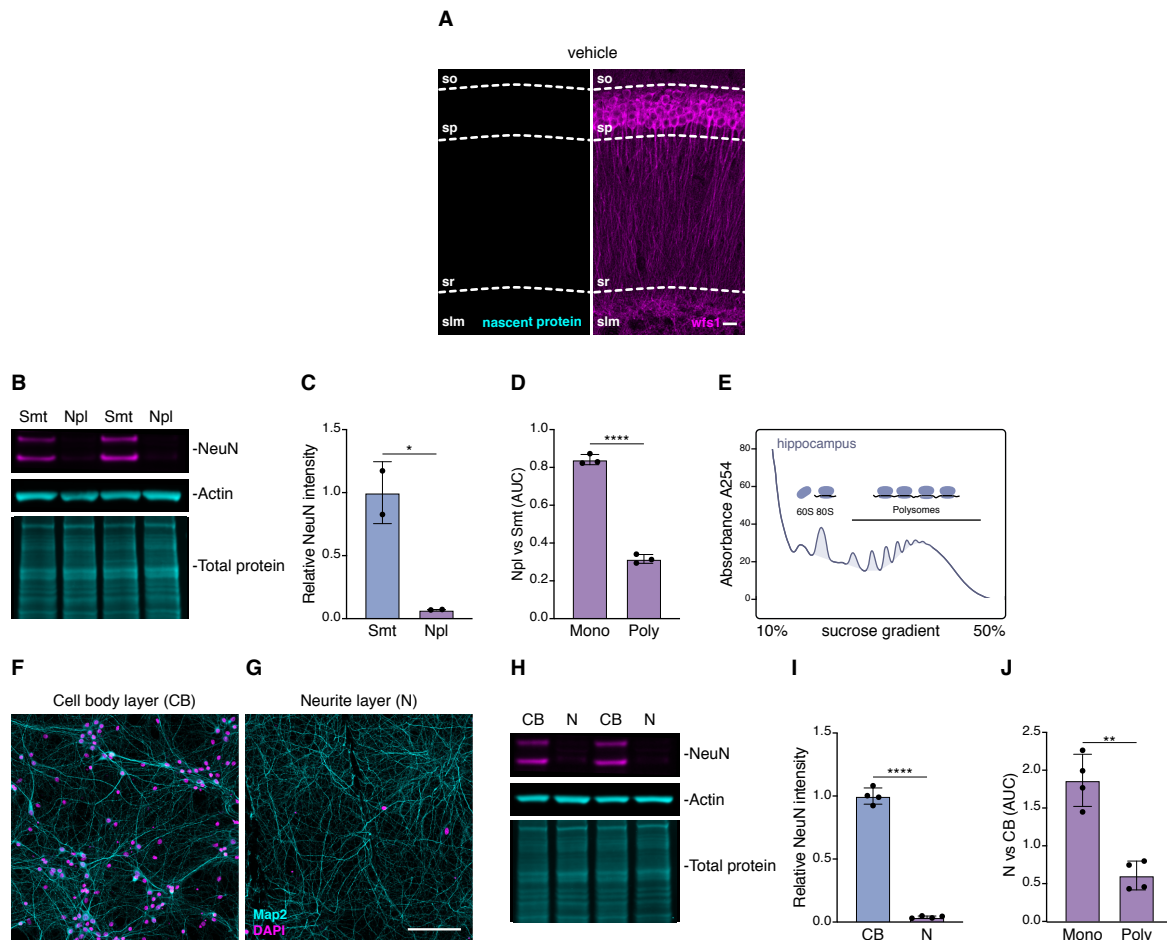
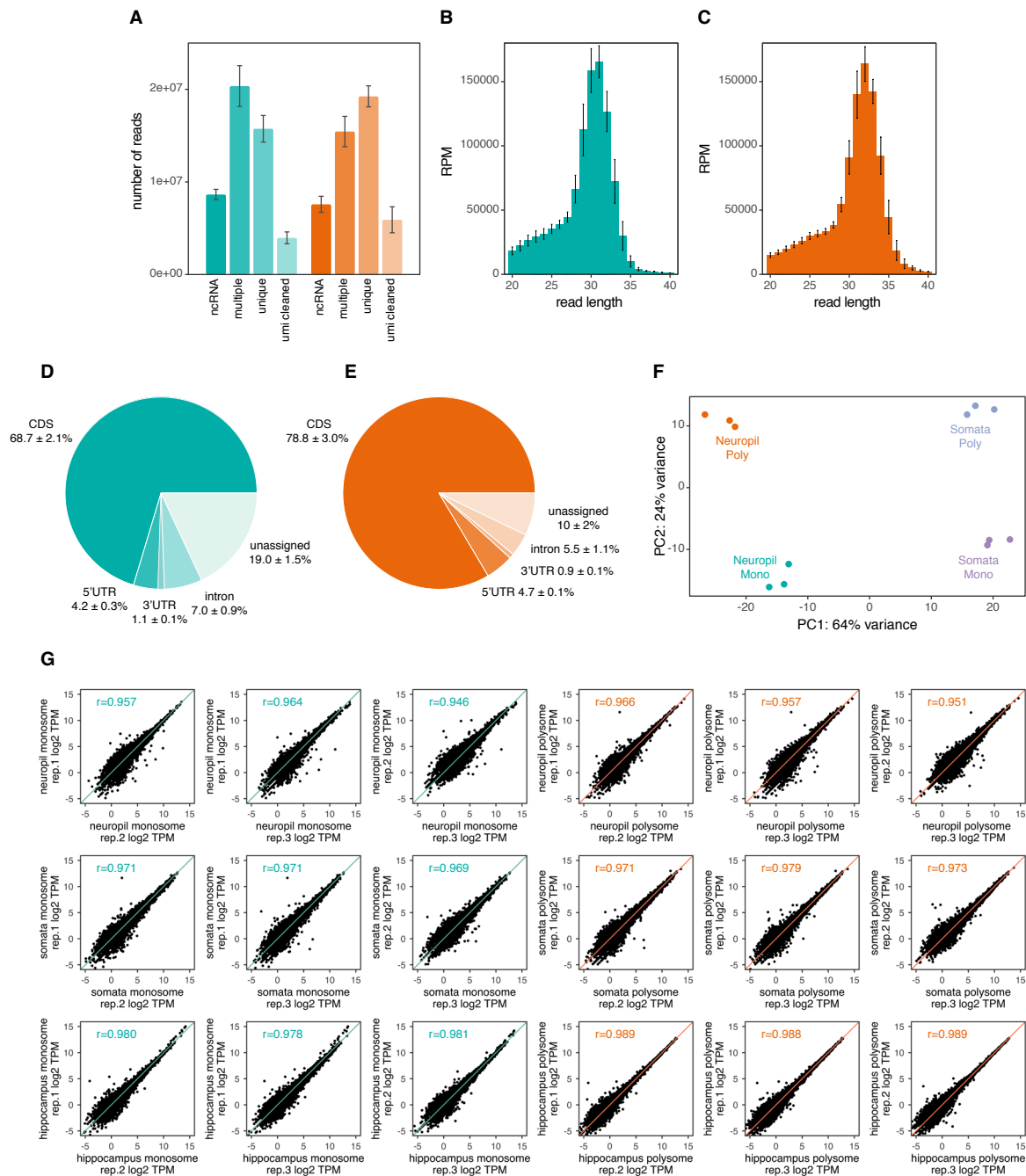**Supplementary figure 1 related to figure 1.**

(A) Immunofluorescence staining of the nascent protein metabolic label puromycin (cyan) and the CA1 pyramidal neuron marker Wfs1 (purple) in hippocampal sections from control mice that received a brief infusion of vehicle into the lateral ventricle. Scale bar = 20 µm. so, *stratum oriens*; sp, *stratum pyramidale*; sr, *stratum radiatum*; slm, *stratum lacunosum moleculare*.

(B and C) Representative western blot **(B)** and quantification **(C)** of the nuclear marker NeuN, actin and total protein in the CA1 somata (Smt) and neuropil (Npl) (n=2). * p = 0.0331, Welch's t-test. **(D)** Comparison between the neuropil:somata ratios of the monosome (Mono) AUC and polysome (Poly) AUC. **** p < 0.0001, Welch's t-test. AUC, area under the curve. **(E)** Representative polysome profile of a whole (non-microdissected) hippocampus.Monosome:polysome ratio = 0.56+/-0.04 (n=3). **(F and G)** Immunofluorescence staining of Map2 (cyan; dendrites) and DAPI (purple; nuclei) in the cell body (CB) **(F)** or neurite (N) **(G)** layer of cortical neurons grown on a microporous membrane. Scale bar = 100 µm. **(H and I)** Representative western blot **(H)** and quantification **(I)** of the nuclear marker NeuN, actin and total protein in the cell body and neurite layer (n=4). **** p < 0.0001, Welch's t-test. **(J)** Comparison between the neurite:cell-body ratios of the monosome (Mono) AUC and polysome (Poly) AUC. ** p = 0.0018, Welch's t-test. AUC, area under curve.
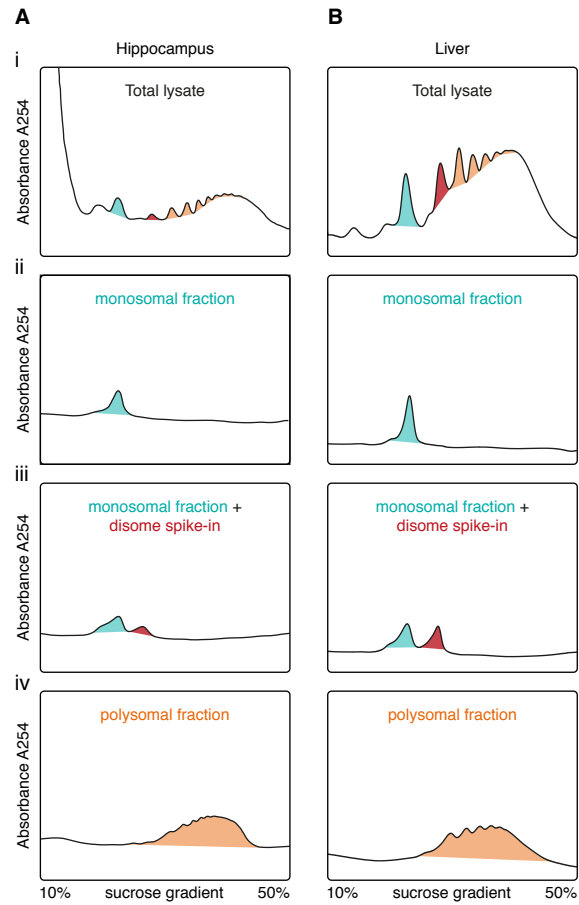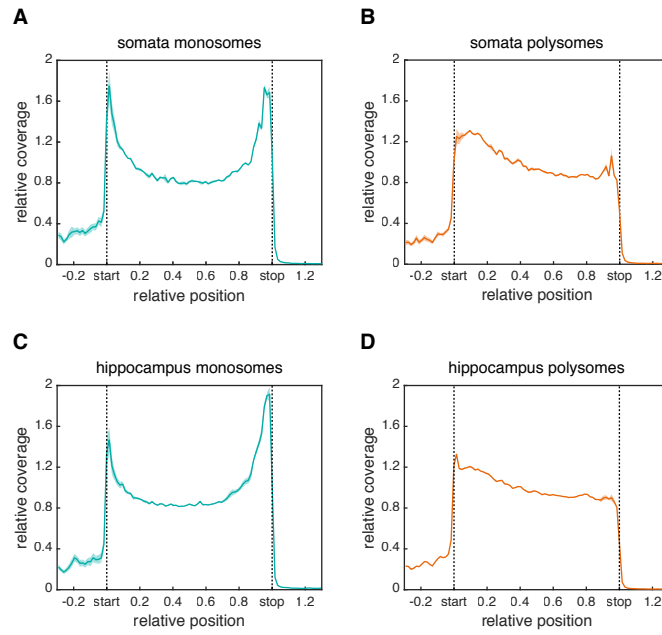
Supplementary figure 2 related to figure 2.
Polysome profiling was performed on hippocampal **(Ai)** or liver **(Bi)** lysates. The monosomal (cyan), disomal (red) and polysomal (orange) fractions were collected. Monosomal **(ii)**, monosomal + disomal **(iii)** or polysomal **(iv)** fractions were then re-separated on a sucrose gradient. The purity of the isolated fractions is demonstrated by the lack of disomes or polysomes in the monosome sucrose gradient profiles **(Aii and Bii)** or monosome in the polysome sucrose gradient profile **(Aiv and Biv)**. Polysome profiling detects potential contaminations of the monosome fraction **(Aiii and Biii)**.
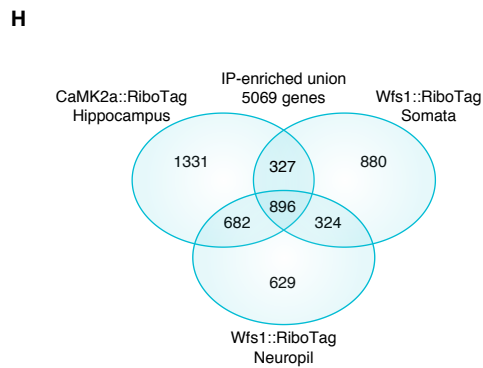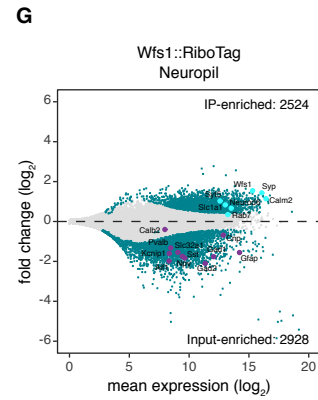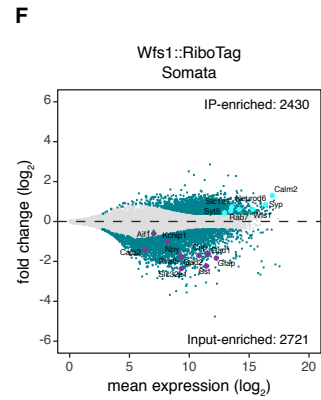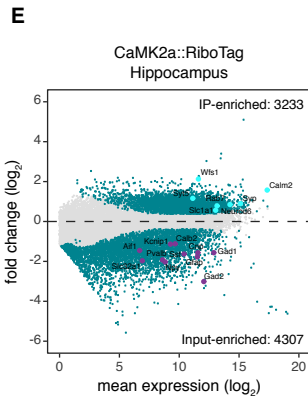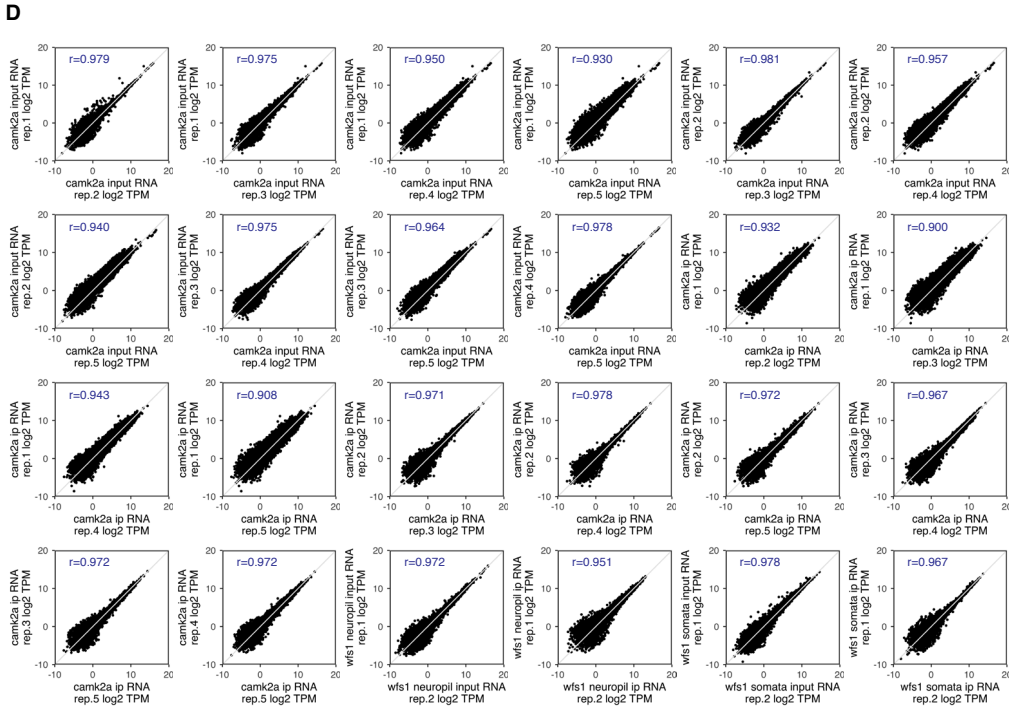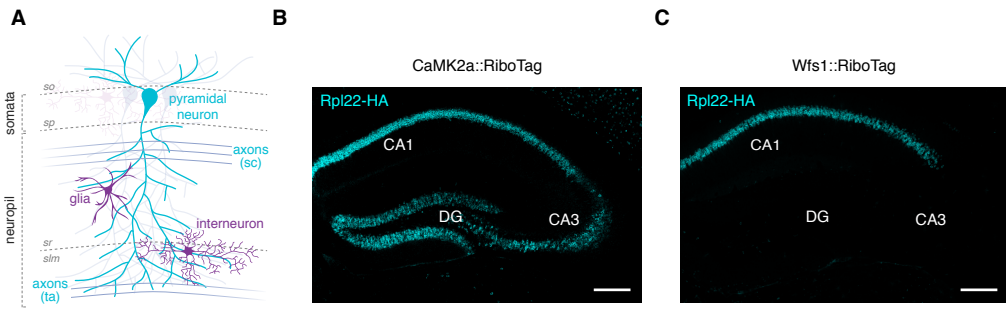
Supplementary figure 3 related to figure 2.
(A) Footprint read count by alignment fate (ncRNA, non-coding RNA; umi, unique molecular identifier; multiple, secondary alignment; unique, primary alignment) in all monosome (cyan) or polysome (orange) samples used in this study. **(B and C)** Distribution of footprint read lengths obtained in monosome **(B)** or polysome **(C)** libraries. **(D and E)** Fraction of monosome **(D)** or polysome **(E)** footprint reads aligning to various genomic features including the 5'UTR, CDS, 3'UTR and introns. **(F)** PCA analysis representing the between and within group variance of neuropil monosome (cyan) or polysome (orange) and somata monosome (purple) or polysome (blue) footprint samples. **(G)** Scatter plots with Pearson's r correlation between biological replicates of hippocampus, somata and neuropil monosome/polysome footprint libraries.
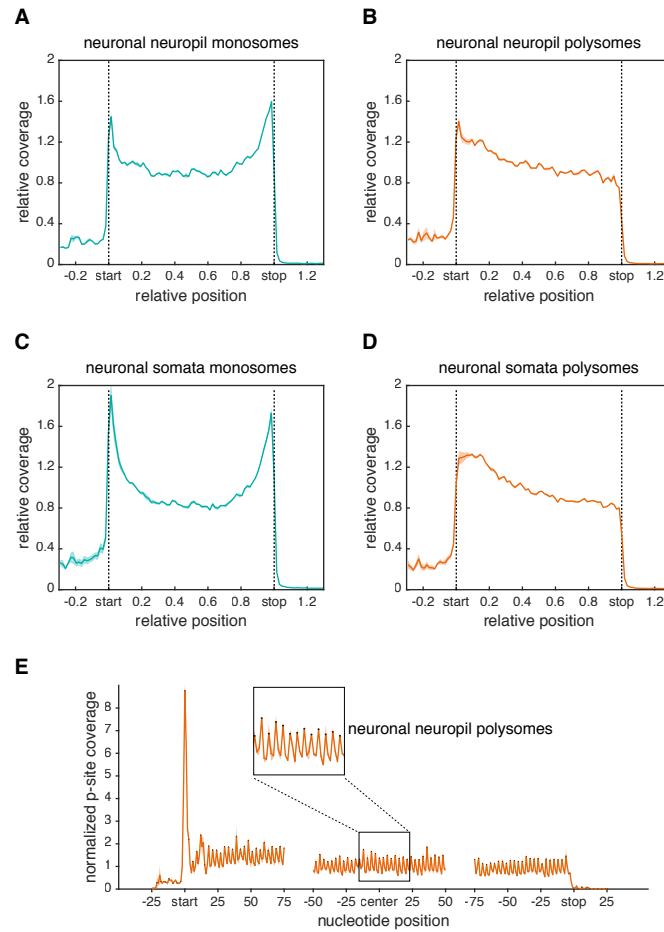
Supplementary figure 4 related to figure 2.
(A to D) Metagene analyses showing the footprint density in the monosome (cyan) or polysome (orange) samples from the somata (for representative polysome profile see Fig. 1C) **(A and B)** or hippocampus **(C and D)** (for representative polysome profile see fig. S1E) throughout the open reading frame. The average relative normalized coverage is plotted per nucleotide position, and the standard deviation is shaded (n=3). Genes were individually normalized.

A

so
somata
sp

pyramidal
neuron

axons
(sc)

glia

neuropil

interneuron

sr
slm

axons
(ta)

B

CaMK2a::RiboTag

Rpl22-HA

CA1

DG   CA3

C

Wfs1::RiboTag

Rpl22-HA

CA1

DG   CA3

D

E

CaMK2a::RiboTag
Hippocampus

IP-enriched: 3233

Input-enriched: 4307

F

Wfs1::RiboTag
Somata

IP-enriched: 2430

Input-enriched: 2721

G

Wfs1::RiboTag
Neuropil

IP-enriched: 2524

Input-enriched: 2928

H

CaMK2a::RiboTag
Hippocampus

IP-enriched union
5069 genes

Wfs1::RiboTag
Somata

1331

327

880

682

896

324

629

Wfs1::RiboTag
Neuropil

I

CA1 Pyramidal

S1 Pyramidal

Interneuron

Astrocyte

Oligodendrocyte

Microglia

Endothelial

Ependymal

Mural

IP-enriched
Input-enriched

Supplementary figure 5 related to figure 2.
(A) Scheme of the CA1 hippocampal area. The somata layer (sp) contains the cell bodies of CA1 pyramidal neurons (cyan). The neuropil layer (sr + slm) contains dendrites from pyramidal neurons (cyan) as well as axons (Schaffer collaterals (sc) + temporoammonic path (ta)). The somata and neuropil layers also contain interneurons and glia (purple). so, *stratum oriens*; sp, *stratum pyramidale*; sr, *stratum radiatum*; slm, *stratum lacunosum moleculare*. **(B and C)** Immunofluorescence staining of Rpl22-HA (anti-HA antibody; cyan) in hippocampal sections from Camk2aCre::RiboTag **(B)** and Wfs1Cre::RiboTag mice **(C)**. CA1, *cornu ammonis* 1; CA3, *cornu ammonis* 3; DG, *dentate gyrus*. Scale bar = 200 µm. **(D)** Scatter plots with Pearson's r correlation between biological replicates of whole hippocampi from Camk2aCre::RiboTag mice (n=5); and somata or neuropil from Wfs1Cre::RiboTag mice (n=2). **(E - G)** MA plots (the average, A, of the log read counts versus the differences in the log read counts, minus, M) showing differentially expressed transcripts between Rpl22-HA immunoprecipitation (IP) and input samples from: **(E)** whole hippocampi of Camk2aCre::RiboTag mice (n=5); **(F)** somata or **(G)** neuropil of Wfs1Cre::RiboTag mice (n=2). Cyan dots indicate the transcripts significantly enriched in the IP or input (DESeq2 with a threshold of 0.05 on the adjusted *p*-value and a 30%-fold-enrichment). Gray dots represent the non-enriched transcripts. Colored dots highlight markers for excitatory neurons (*Wfs1*, *Slc1a1*, *Calm2*, *Syp*, *Neurod6*, *Rab7* and *Syt5*); astrocytes (*Gfap*); microglia (*Aif1*); oligodendrocytes (*Cnp*) or different interneuron categories (*Gad1*, *Gad2*, *Kcnip1*, *Calb2*, *Npy*, *Pvalb*, *Slc32a1*, *Sst*). **(H)** Venn diagram comparing the transcripts significantly enriched in the Rpl22-HA IP from three different sources: the hippocampus of Camk2aCre::RiboTag mice, the microdissected somata or the neuropil of Wfs1Cre::RiboTag mice. A classifier to identify excitatory neuron-enriched genes was developed based on the union of the three datasets (5069 genes). **(I)** Observed-to-expected ratio of genes enriched in the Rpl22-HA IP (cyan) or the input (purple) and previously associated with different hippocampal cell-types by a single-cell study (*20*). Numbers within the bars indicate the *p*-values for the enrichment (using a hypergeometric test).
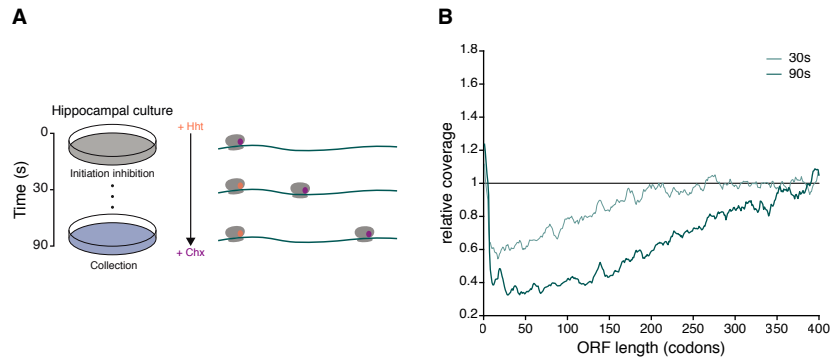
Supplementary figure 6 related to figure 2.
(A-D) Metagene analyses showing the footprint density across neuronal transcripts in the monosome (cyan) or polysome (orange) samples from the neuropil **(A and B)** and somata **(C and D)**. The average relative normalized coverage is plotted per nucleotide position, and the standard deviation is shaded (n=3). Genes were individually normalized. **(E)** Metagene analyses showing the P-site coverage of neuronal transcripts in the neuropil polysome sample. The average normalized coverage is plotted per nucleotide position around the 5' end (start), central portion (center) and 3'end (stop) of the ORF. The standard deviation is shaded (n=3).
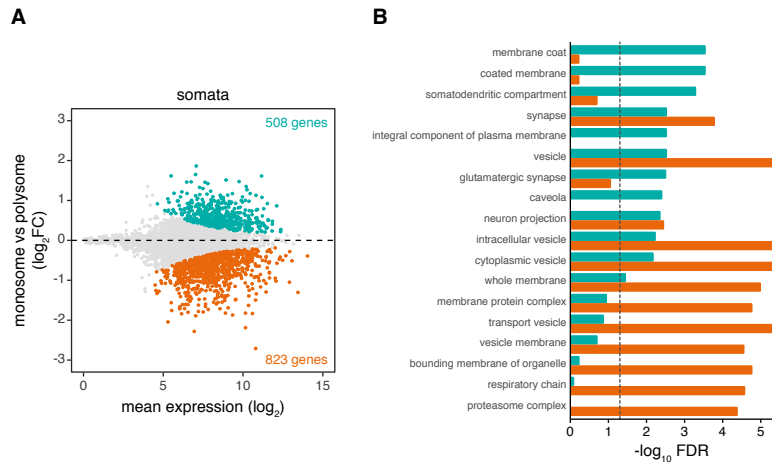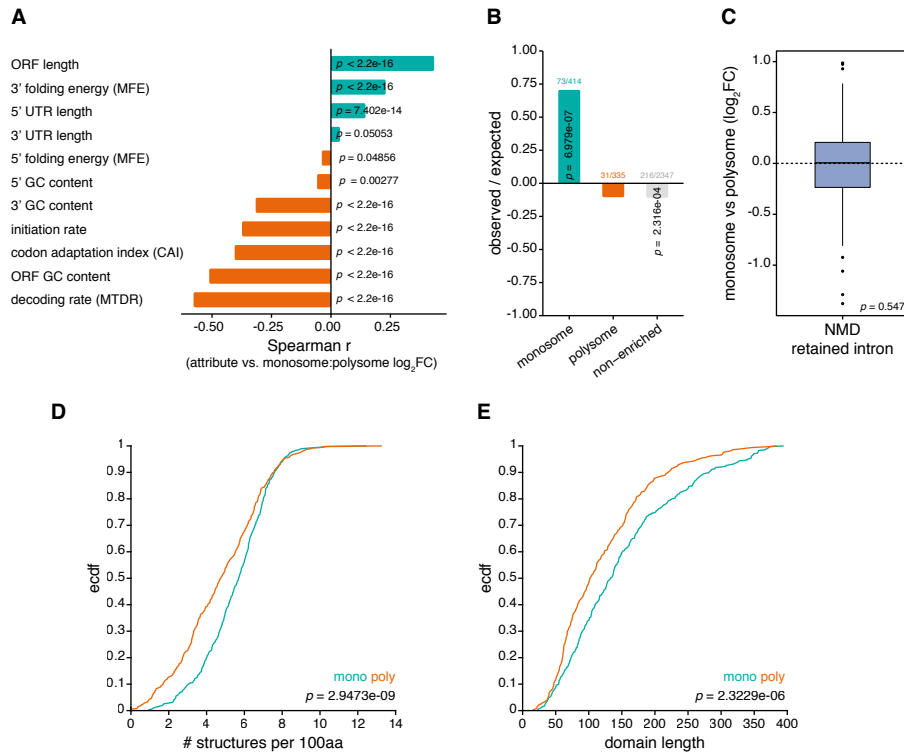
Supplementary figure 7 related to figure 3.
(A) MA plot (the average, A, of the log read counts versus the differences in the log read counts, minus, M) showing transcripts with differential monosome (cyan) or polysome (orange) footprint coverage in the central portion of the ORF (region spanning 15 codons from the start site to 5 codons before the stop site) in the somata. **(B)** GO terms representing the top ten significantly enriched protein function groups for monosome (cyan) or polysome (orange)-enriched transcripts in the somata.
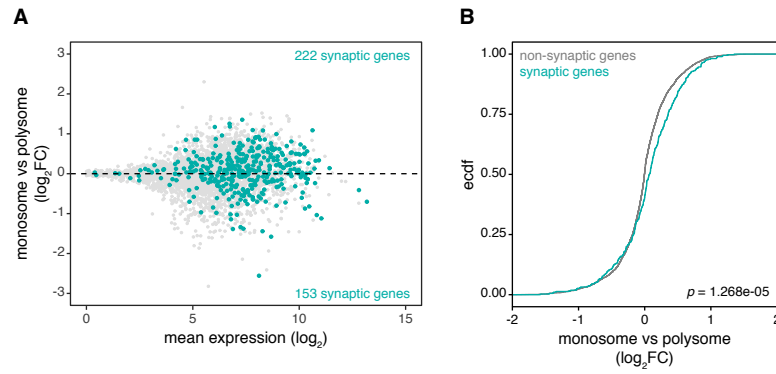
Supplementary figure 8 related to figure 3.
(A) Schematic of the in vivo run-off elongation experiment in rat hippocampal cultures. **(B)** Meta-gene analysis of run-off elongation on monosome-preferring transcripts. Ribosome depletion is shown for a subset of transcripts exhibiting significant monosome preference in both whole hippocampi and hippocampal cultures (see Methods). Ribosome densities of the samples treated with harringtonine for 30 and 90 sec were normalized to the untreated control (n=3).
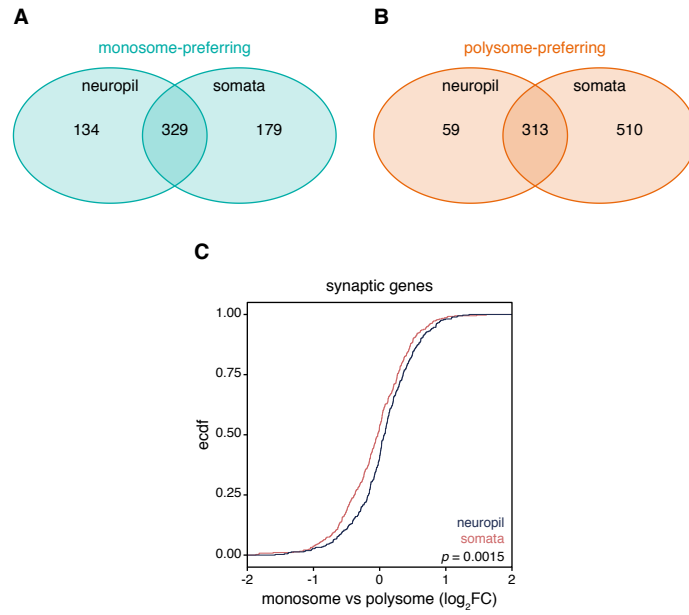
Supplementary figure 9 related to figure 3.
(A) Transcript attributes were correlated with the neuropil monosome:polysome fold-changes (FC). Positive (cyan) and negative (orange) Spearman correlation coefficients and *p*-values are shown. MFE, minimum free energy; CAI, codon adaptation index; MTDR, mean typical decoding rate. **(B)** Observed-to-expected ratio of monosome (cyan), polysome (orange)-and non-preferring (gray) transcripts containing uORFs. Numbers of uORF-containing transcripts per gene subset are shown above the bars. Numbers within the bars indicate the significant *p*-values for over- and underrepresentation (using a hypergeometric test). **(C)** Boxplot of monosome:polysome fold-changes for transcripts classified as biotypes 'non-sense mediated decay (NMD)' or 'retained intron' by Ensembl ($p = 0.547$, one-sample Wilcoxon signed rank test, $\mu = 0$). **(D and E)** Cumulative distribution frequency depicting the number of structured (α-helix and β-strand) regions per 100aa ($p = 2.9473e-09$, Kolmogorow-Smirnow-Test) **(D)** or the length of structural domains ($p = 2.3229e-06$, Kolmogorow-Smirnow-Test) **(E)** in proteins encoded by monosome (cyan) -or polysome (orange) -preferring transcripts in the neuropil.
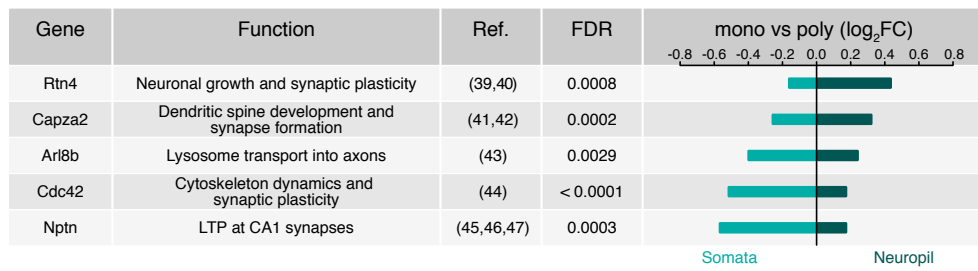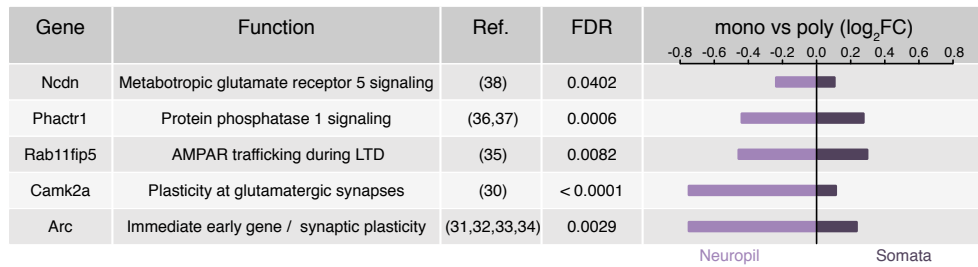
Supplementary figure 10 related to figure 3.
(A) MA plot (the average, A, of the log read counts versus the differences in the log read counts, minus, M) showing the $\log_2$ fold-changes between the monosome or polysome footprint coverage in the central portion of the ORF (region spanning 15 codons from the start site to 5 codons before the stop site) in the neuropil. Cyan dots highlight synaptic genes (SynGO annotation).
(B) Cumulative distribution frequency depicting the monosome:polysome $\log_2$ fold-changes for synaptic (cyan) and non-synaptic (gray) genes. $p = 1.268e-05$, Kolmogorov-Smirnov-Test.

A monosome-preferring

neuropil | somata
134 | 329 | 179

B polysome-preferring

neuropil | somata
59 | 313 | 510

C synaptic genes

neuropil
somata
$p = 0.0015$

monosome vs polysome ($\log_2$FC)

Supplementary figure 11 related to figure 4.
(A and B) Venn diagrams representing the overlap of monosome- **(A)** and polysome-preferring **(B)** transcripts between the somata and the neuropil. Numbers were obtained from the DESeq2 analysis in Fig. 3A and fig S7A. **(C)** Cumulative distribution frequency depicting the mono-some:polysome $\log_2$ fold-changes of synaptic transcripts (SynGO annotation) in the somata (gray) and neuropil (black), $p = 0.0015$, Kolmogorov-Smirnov-Test.

A

Gene	Function	Ref.	FDR	mono vs poly (log$_2$FC)
Rtn4	Neuronal growth and synaptic plasticity	(39,40)	0.0008	
Capza2	Dendritic spine development and synapse formation	(41,42)	0.0002	
Arl8b	Lysosome transport into axons	(43)	0.0029	
Cdc42	Cytoskeleton dynamics and synaptic plasticity	(44)	< 0.0001	
Nptn	LTP at CA1 synapses	(45,46,47)	0.0003	

Somata   Neuropil

B

Gene	Function	Ref.	FDR	mono vs poly (log$_2$FC)
Ncdn	Metabotropic glutamate receptor 5 signaling	(38)	0.0402	
Phactr1	Protein phosphatase 1 signaling	(36,37)	0.0006	
Rab11fip5	AMPAR trafficking during LTD	(35)	0.0082	
Camk2a	Plasticity at glutamatergic synapses	(30)	< 0.0001	
Arc	Immediate early gene / synaptic plasticity	(31,32,33,34)	0.0029	

Neuropil   Somata

Supplementary figure 12 related to figure 4.
(A and B) Examples of transcripts encoding plasticity proteins that exhibit polysome preference in the somata but monosome preference in the neuropil (Fig. 4A quadrant 2) **(A)** or vice-versa (quadrant 4) **(B)**.
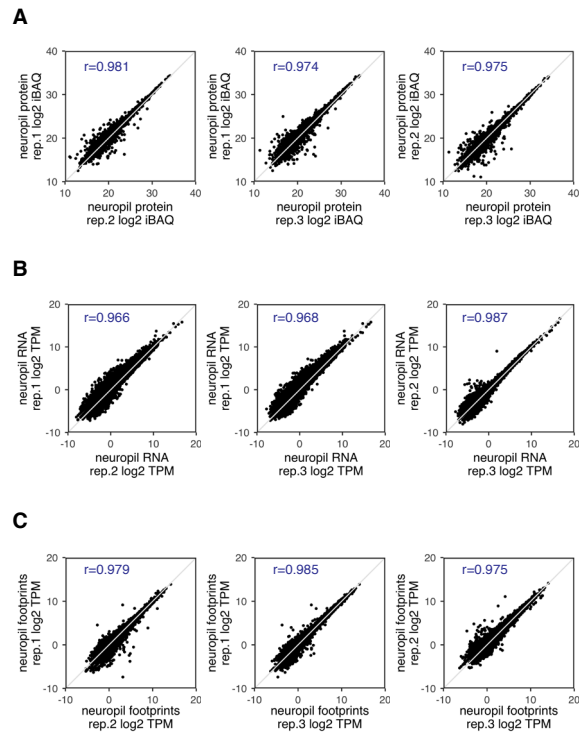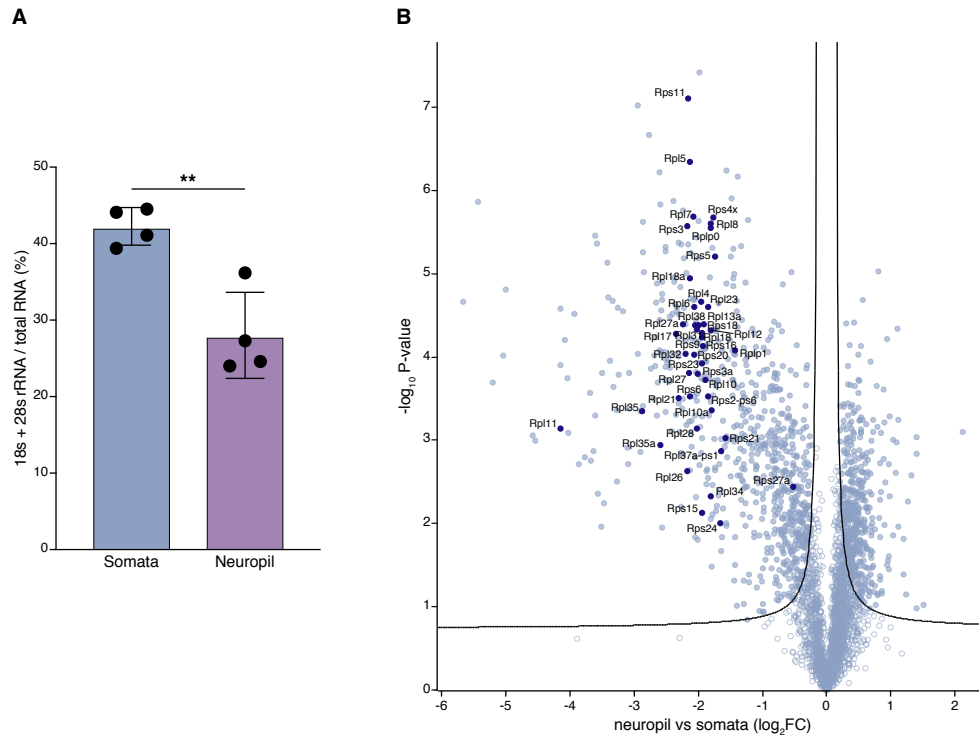
Supplementary figure 13 related to figure 5.
(A, B and C) Scatter plots with Pearson's r correlation of protein ($\log_2$-transformed iBAQ values) **(A)**, RNA ($\log_2$-transformed transcripts per million (TPM)) **(B)** and total footprint (without biochemical fractionation) ($\log_2$-transformed TPMs) **(C)** measurements from the neuropil of three biological replicates.
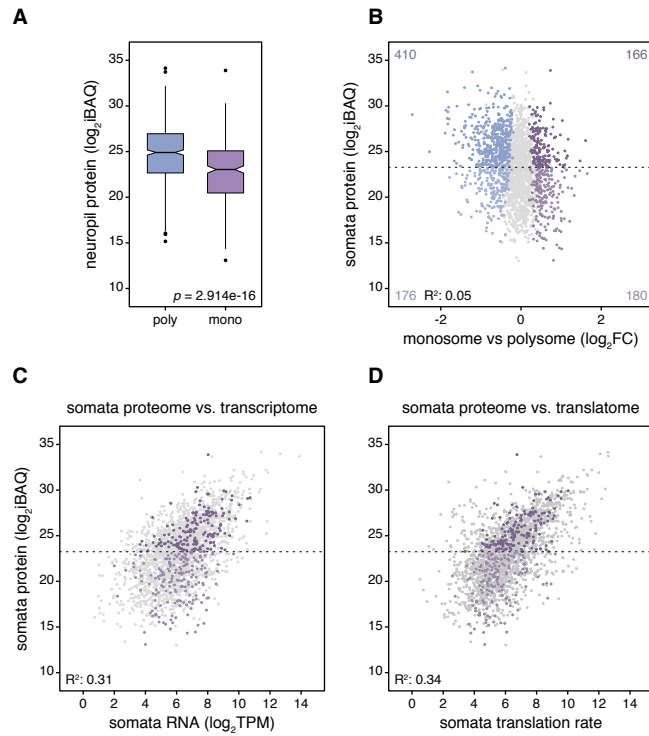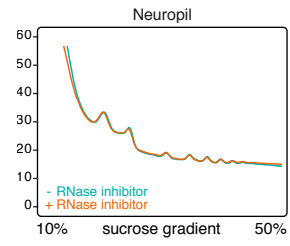
Supplementary figure 14 related to figure 5.
(A) Box plots of protein (log$_2$iBAQ) measurements in the somata for monosome- (mono, purple) or polysome- (poly, blue) enriched genes (p = 2.914e-16, Wilcoxon rank-sum test). Of 508 and 823 monosome-and polysome-preferring transcripts in the neuropil, 346 and 586 respectively, passed the stringent proteomics filtering criteria (see Methods). **(B)** A scatter plot of the somata protein abundance (log$_2$iBAQ) versus monosome:polysome fold-changes for monosome (purple)-, polysome (blue) -and non-enriched (gray) genes (R^2 = 0.05, p = 2.944e-11). The dashed line indicates the mean log$_2$ iBAQ value. Monosome-preferring transcripts encoding proteins with abundances greater than average are highlighted by dark purple dots (mono-high) **(C and D)**. The proteome correlates with the transcriptome and translatome in the somata. A scatter plot of the somata protein abundance (log$_2$iBAQ) versus RNA (log$_2$TPM) (R^2 = 0.31, p < 2.2e-16) **(C)** and translation rate (obtained from total footprints, without biochemical fractionation) (R^2 = 0.34, p < 2.2e-16) **(D)** measurements for all genes. Monosome-preferring genes encoding high-abundance proteins are highlighted by dark purple dots.

A

B

Supplementary figure 15 related to figure 5.
(A) Percentage of 18S and 28S rRNA relative to total RNA in the somata versus neuropil (n=4).
** p = 0.0092, Welch's t-test. **(B)** Vulcano plot representing neuropil versus somata $\log_2$ fold-changes. Dark blue dots highlight ribosomal proteins, which are enriched in the somata.

Supplementary figure 16 related to figure 2.
Polysome profiling was performed on the CA1 neuropil in the presence (orange) or absence (cyan) of RNase inhibitors.